Applied Thermal Engineering 247 (2024) 122984

Contents lists available at ScienceDirect

Applied Thermal Engineering

journal homepage: www.elsevier.com/locate/apthermeng

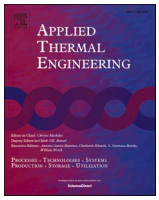

Research Paper

Solar cavity receiver for melting zinc metal

Pieter J.A. Bezuidenhout [a,b,c], Willem G. le Roux [a,*]

[a] Department of Mechanical and Aeronautical Engineering, University of Pretoria, South Africa
[b] Pyrometallurgy Division, Mintek, South Africa
[c] Tenova Pyromet, South Africa

ARTICLE INFO

Keywords:
Cavity receiver
Solar dish
Concentrated solar power
Zinc melting
Renewable energy

ABSTRACT

Concentrating solar power technologies can be applied to reduce the cost and carbon footprint of zinc melting processes. This study aims to improve the knowledge related to small-scale solar melting using a dish concentrator. This technology can be applied to zinc production as well as a range of small-scale applications, such as casting, recycling, galvanisation, and thermal storage. An experimental and analytical analysis of a rotating cylindrical cavity receiver for the indirect melting of zinc metal using concentrated solar power is presented. A multi-facet parabolic dish with an incident area of 2.85 m^2 was considered together with a rotating cylindrical cavity receiver. The receiver had an aperture diameter of 0.2 m and the capacity for housing 17 kg of zinc. Five experimental test runs were executed, during which up to 73.5 % of the zinc inventory could be tapped from the receiver in its molten state, and average thermal efficiencies of up to 42 % were achieved. A predictive analytical model considering wind speed, wind direction, and direct normal irradiance was developed and validated against experimental data. A heat transfer efficiency factor was experimentally determined to account for voids in the zinc feedstock. The model was used to predict that approximately 41 kg of molten zinc could be tapped from the experimental setup throughout a typical day with a peak direct normal irradiance of about 900 W/m^2 and an average wind speed below 2 m/s. A case study highlighted that energy savings of 0.6 kWh are achievable per kilogram of zinc processed by concentrated solar power rather than the conventional induction furnace.

1. Introduction

The industrial sector is predicted to be the most significant greenhouse gas producer by 2060 [1]. Process heat represents two-thirds of the industrial energy demand, of which more than 90 % is currently supplied by burning fossil fuels [1]. In this area, numerous opportunities exist for renewable alternatives such as solar thermal energy to revolutionize industrial heat supply and reduce the carbon footprint of conventional industrial processes. The mining industry is of particular interest due to its substantial contribution to global greenhouse gas emissions, and heat applications in this industry are typically categorized as high-temperature applications (>400 °C) [2]. Various authors [3–5] have shown that achieving operating temperatures in excess of 400 °C is possible using concentrated solar power (CSP) technologies, making it an ideal application for providing process heat to this industrial sector. There exist various high-temperature industrial heat applications with the potential to use concentrated solar thermal energy, but for this study, a focus was placed on the melting of zinc metal.

Zinc is deemed essential for modern living and is ranked fourth in terms of all metal production in the world [6]. South Africa houses the 5th largest zinc reserve in the world [7], but at the time of writing, no local beneficiation takes place, with all mined ore being exported. This is mainly due to an expensive and unreliable power network. Most of the primary zinc deposits in South Africa are located in areas with some of the world's best solar irradiance [8,9], allowing for the possibility of linking the beneficiation of this mineral resource to a solar thermal process. By identifying alternative methods of providing the required process heat for zinc processing, local beneficiation of zinc can have a significant impact on the South African economy and allow for micro-processing by local entrepreneurs.

Zinc is the third most widely used non-ferrous metal after copper and aluminium [10,11]. One of the most common methods of producing zinc is the hydro-metallurgical or Roast-Leach-Electrowin (RLE) process, producing about 80 % of the world's zinc [10]. A detailed description of the RLE flowsheet is outlined by van Dyk [11], but it typically consists of a roasting, leaching, solution purification, cooling, electrowinning, and casting step. After the electrowinning process, during which zinc metal is plated to aluminum cathodes, the zinc metal is stripped from the cathodes and remelted at 450 °C, in induction furnaces to produce ingots

* Corresponding author.
E-mail address: willem.leroux@up.ac.za (W.G. le Roux).

https://doi.org/10.1016/j.applthermaleng.2024.122984
Received 6 September 2023; Received in revised form 26 February 2024; Accepted 16 March 2024
Available online 17 March 2024

Nomenclature

A_{ap}	Area of the receiver aperture $[m^2]$
A_{cav}	Surface area of the cavity $[m^2]$
A_D	Dish incident reflective area $[m^2]$
c	Heat transfer efficiency constant
C	Constant for cylinders in cross-flow
$c_{p_{liquid-Zn}}$	Specific heat capacity of molten zinc $[J/K \bullet kg]$
$c_{p_{solid-Zn}}$	Specific heat capacity of solid zinc $[J/K \bullet kg]$
$c_{p_{steel}}$	Specific heat capacity of mild steel $[J/K \bullet kg]$
d	Aperture diameter $[m]$
D_{ap}	Diameter of the receiver aperture $[m]$
D_D	Dish diameter $[m]$
D_i	Receiver cavity inner diameter $[m]$
D_{ins}	Outer diameter of insulation material $[m]$
f_D	Dish local focal length $[m]$
f_s	Shading factor
g	Gravitational acceleration $[m/s^2]$
Gr_L	Grashof number
h_D	Height of parabola $[m]$
h_{in}	Internal convection heat transfer coefficient of the receiver $[W/m^2 \bullet K]$
h_o	Convection heat transfer coefficient on outer surface $[W/m^2 \bullet K]$
I	Solar direct normal irradiance (DNI) $[W/m^2]$
k_{ins}	Thermal conductivity of insulation material $[W/m \bullet K]$
l_c	Aperture-cavity radius ratio
L_{rec}	Receiver characteristic length $[m]$
m	Constant for cylinders in cross-flow
m_{steel}	Mass of receiver steel $[kg]$
m_{zn}	Mass of zinc inventory/batch $[kg]$
$m_{zn,liquid}$	Mass of zinc inventory/batch in molten form $[kg]$
Nu	Nusselt number for convection inside receiver
$Nu_{cav,forc}$	Nusselt number for forced convection from the cavity
$Nu_{cav,nat}$	Nusselt number for natural convection from the cavity
$Nu_{D,forc}$	Nusselt number for forced convection over receiver cylinder
$Nu_{D,nat}$	Nusselt number for natural convection over receiver cylinder
p	Coefficient for calculating Nusselt number for forced convection
$P(\theta)$	Function of receiver tilt angle
Pr	Prandtl number
q	Coefficient for calculating Nusselt number for forced convection
$\dot{Q}_{net}$	Net theat input rate into zinc $[W]$
$\dot{Q}_{ap,in}$	Heat input rate collected at receiver aperture $[W]$
$\dot{Q}_{cond,loss}$	Conduction heat loss rate $[W]$
$\dot{Q}_{conv,loss}$	Convection heat loss rate $[W]$
$\dot{Q}_{rad,loss}$	Radiation heat loss rate $[W]$
$\dot{Q}_{rad,em}$	Rate of radiation losses due to emissivity $[W]$
$\dot{Q}_{rad,ref}$	Rate of radiation losses due to reflection $[W]$
r	Coefficient for calculating Nusselt number for forced convection
$r_{i,ins}$	Inner radius of insulation material $[m]$
$r_{o,ins}$	Outer radius of insulation material $[m]$
$Ra_{D,ins}$	Rayleigh number on the insulation outer surface
R_{conv}	Convection resistance $[K/W]$
$Re_{D,ins}$	Reynolds number for flow over insulation material
R_{ins}	Thermal resistance of insulation material $[K/W]$
R_{tot}	Combined thermal resistance $[K/W]$
s	Coefficient for calculating Nusselt number for forced convection
t	Coefficient for calculating Nusselt number for forced convection
T_{bulk}	Bulk mean temperature inside the cavity $[K]$
T_{cav}	Receiver cavity temperature $[K]$
T_∞	Ambient temperature $[K]$
$T_{Zn,ave}$	Average zinc temperature $[K]$
ν_{air}	Kinematic viscosity of air $[m/s^2]$
V_{wind}	Wind speed $[m/s]$
Zn	Zinc

Greek symbols

α_{cav}	Cavity absorptance
α_{eff}	Effective absorptance
β	Receiver inclination angle $[deg]$
β_v	Volumetric thermal expansion coefficient $[1/K]$
ε_{cav}	Emissivity of cavity
ε_{eff}	Effective cavity emissivity
λ_{zn}	Latent heat of fusion of zinc $[J/kg]$
$\varphi_{rim,D}$	Dish global rim angle $[deg]$
$\eta_{th,rec}$	Thermal efficiency of the receiver [%]
η_D	Dish reflector efficiency [%]
θ	Receiver tilt angle $[deg]$
Γ	Intercept factor
μ_{air}	Ambient air viscosity $[kg/m \bullet s]$
ρ_{air}	Density of air $[kg/m^3]$
ρ_D	Facet reflectivity [%]
φ	Incident angle of wind direction relative to receiver aperture $[deg]$
σ	Stefan-Boltzmann constant $[W/m^2K^4]$

Subscripts

air	Air properties
ave	Average
ap	Aperture
D	Dish
cav	Cavity
cond	Conduction
conv	Convection
eff	Effective
em	Emissivity
forc	Forced
i	Inner
in	Internal
∞	Ambient conditions
ins	Insulation material
L	Length of receiver
nat	Natural
rad	Radiation
rec	Receiver
ref	Reflectivity
s	Surface
t	Time
tot	Total
o	Outer
wall	Available on the receiver cavity wall
zn	Zinc

Abbreviations

CFD	Computational Fluid Dynamics
CSP	Concentrated Solar Power
CSV	Comma Separated Values
DAQ	Data Acquisition
DNI	Direct Normal Irradiance
HFR	Heliostat Field Reflector

NEMA	National Electrical Manufacturers Association	STC	Solar Thermal Collectors
PDR	Parabolic Dish Reflector	TC	Thermocouple
RLE	Roast-Leach-Electrowin	VNC	Virtual Network Computing
SAURAN	South African Universities Radiometric Network		

[11]. The significant energy demand of the RLE process, as a whole, makes it unlikely to be satisfied by current CSP technologies, however, a desktop study by Sithole et al. [12] has shown that solar thermal heating can reduce the energy cost of the casting process by more than 50 % and the indirect CO_2 emissions by up to 80 %. The casting step in the conventional zinc metal flowsheet has been identified as a good starting point to achieve the goal of local beneficiation of zinc ore in South Africa through the use of CSP.

Two-axis tracking, solar thermal collector (STC) technologies have been shown to achieve operating temperatures in the range of 420 °C [13], which is the melting point of zinc metal. The two most common STC technologies that fall under this category are heliostat field reflectors (HFR) and parabolic dish reflectors (PDR) [3]. PDR is widely regarded as the most efficient solar concentrating technology [14], not only because of excellent optical performance, but also because mass-production techniques can be applied to decrease the production cost of these units [14]. Considering that a single dish represents a full CSP system, operating temperatures similar to HFR are achievable, but with a significantly smaller footprint and at lower cost.

When designing a solar receiver for a focal point STC technology application, several thermal and mechanical design considerations need to be evaluated and considered. At elevated temperatures, the most common heat loss from a receiver is radiation heat losses, followed by convective heat losses, and the smallest fraction is accounted for by conductive heat losses [15–17]. Bellos et al. [18] and Kasaeian et al. [17] provided a detailed analysis and review of cavity receiver designs for PDR and indicated that cavity receivers are some of the most common receiver types used in combination with PDR. Cavity receivers achieve high optical efficiencies by trapping incident solar radiation inside the cavity, and by doing so, the effective absorbance of the receiver increases [18]. The findings by Bellos et al. [18] and Kasaeian et al. [17] indicate that a cylindrical-conical cavity design generates some of the highest thermal and exergy efficiencies, followed by spherical and cylindrical cavities. Work by Demirtaş and Özcan [19] on melting aluminium using a conically shaped cavity receiver has reported a thermal efficiency of 22 %. In the work of Demirtaş and Özcan [19], a rectangular aluminium plate sample was positioned inside the conical-shaped cavity and directly exposed to concentrated solar radiation.

The air flow and heat transfer characteristics within a closed cavity typically depend on variables such as the temperature inside the cavity, the cavity shape and the inclination angle of the cavity [20,21]. For open-cavity receivers, wind speed and direction as well as wind shielding affects convection heat losses [22]. Natural convection from cavity receivers is reasonably well understood and backed by good experimental results as published by Taumoefolau et al. [23], Yazdanipour et al. [24], and Abbasi-Shavazi et al. [25]. Ma [22] found that forced convection as a result of high wind speeds, can be as high as three times the maximum level of natural convection. This finding highlighted the need to include forced convection losses when evaluating a receiver design that will be exposed to environmental conditions. Several authors [22,26–31] have considered the effect of wind speed on convection heat losses, but these authors only considered wind speed with no wind direction, or wind speed and only two receiver orientations (vertical and horizontal). Limited studies have investigated the effect of wind speed together with wind yaw angle. Authors such as Lee et al. [30] and Wu et al. [32] have experimentally investigated the effect of wind speed and yaw angle on heat losses, but this was done at either lower temperatures than what this study will achieve or only at selected receiver inclination angles. Reddy et al. [27] developed a numerical model for a range of receiver inclinations, wind speeds, and directions as well as for cavity temperatures of up to 600 °C.

Kasaeian et al. [17] found that the optimum cavity length is equal to the cavity aperture for cylindrical and rectangular cavities. Other design considerations include a concentrating cone on the cavity aperture [33], which can aid in solar radiation collection, and modifying the cavity aperture by adding plate fins [34]. Another critical design consideration is that of the material of construction, and based on the requirement for this study and the need to contain molten zinc, galvanizing zinc kettles were investigated. Due to the aggressive nature of liquid zinc towards steel, zinc kettles are usually made of low-carbon, low-silicon steel [35–37].

1.1. Main contribution and novelty of this work

At the time of writing, minimal literature could be found on the melting of zinc metal using concentrated solar power, and no literature of experimental data demonstrating this concept. This study set out to experimentally demonstrate the melting of zinc, using only concentrated solar power, in order to provide valuable insight into the operational requirements of this technology application. The technology can be applied to a range of applications, including but not limited to: casting (including small-scale battery technology and ingot casting as part of the RLE process), metal recycling, galvanisation, and small-scale thermal storage. Zinc is currently melted using gas-fired, coal-fired, and electric furnaces, which can result in significant energy costs and CO_2 emissions [8,38], especially for galvanization, the most common application of zinc [39]. The study will serve as a starting point to demonstrate the potential for using CSP to beneficiate local resources, such as the example of zinc ore in the South African context, and for the use in other melting applications. An analytical model was developed to serve as a desktop tool for the further development of this technology, and the accuracy thereof was demonstrated by comparison with experimental data, providing the necessary confidence in the model.

2. Experimental setup

To investigate the potential for melting zinc metal using CSP, an experimental setup [40] was constructed to evaluate this concept under real environmental conditions. In this section, the design considerations pertaining to the experimental setup are discussed, describing the design in sufficient detail. The experimental setup, which included a multi-facet dish assembly, a solar receiver, a drive system, a data logging system, and a tracking system, are shown in Fig. 1.

The multi-facet modular dish is referred to as the solar collector or solar dish. In this design, the solar receiver not only absorbed the concentrated solar radiation but also housed the zinc metal inventory. Using a drive system, the solar receiver was rotated to limit the possibility of hot spot formation inside the receiver and improve heat transfer and mixing of the zinc feedstock. The solar dish and receiver assembly were allowed to face the sun for the duration of the testing period by adjusting the tracking system in both the azimuth and elevation direction. The receiver cavity temperature and the temperature of the zinc metal were remotely monitored and used as an indication as to when the zinc inventory was fully molten and ready to be tapped from the receiver. In each of the following sections, each of these individual subsystems are discussed in greater detail.

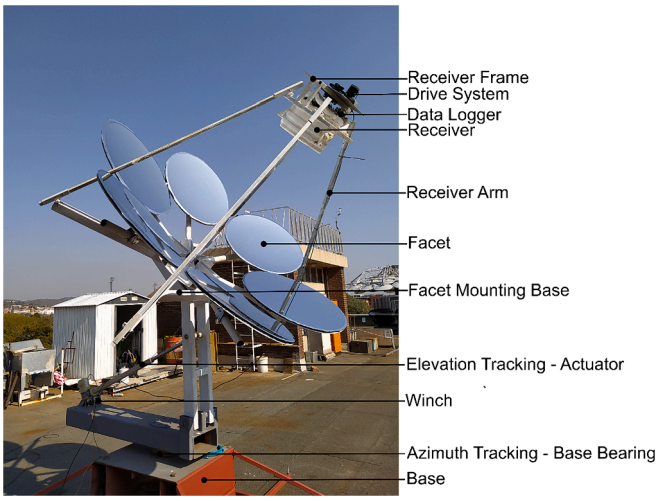

Fig. 1. Experimental setup showing all the individual sub-components.

2.1. Solar dish design

The solar dish was made up of 6 smaller mirror facets that work independently to concentrate incoming solar radiation to a single focal point, at which the receiver was positioned. Each mirror facet was constructed by stretching and sticking a sheet of EverBright mirror film [41] to the rim of an ordinary television satellite dish. This assembly method and a pneumatic valve fitted to the back of the satellite dish allowed for a vacuum to be drawn and maintained behind the membrane. By pulling a vacuum behind the membrane, the reflective surface of the membrane could be formed into a concave shape that aided in focusing the collected solar radiation [42–44].

The inner dimensions of each facet were measured to be 820 mm × 757.5 mm [42], resulting in an elliptical shape rather than a circle. Zanganeh et al. [45] have shown that this characteristic can be used as an advantage. By tilting the elliptically-shaped facet to face the receiver, as done in the multi-facet design, a near circular image will be projected onto the receiver aperture [45]. This will increase the intercept factor and the concentration ratio of the assembly [45]. Each facet was tilted 13.6° upward from the horizontal plane to achieve the above-mentioned projection characteristic. A rim angle was decided based on the flux distribution achieved, as a result, on the inside of the cavity wall (see Section 2.2 for the description of the solar receiver). An effective rim angle of 40°, as illustrated in Fig. 2, allowed for sufficient penetration onto the receiver cavity while maintaining a relatively short focal length. As the focal length increased, the receiver arm (the structural steel section that supports the receiver) would also increase in length which could result in the dish assembly becoming top-heavy or introduce unwanted movement at the receiver end during tracking. Each facet was positioned at $D_D/2 = 0.8$ m from the centroid of the global dish assembly, which resulted in an effective dish diameter of $D_D = 1.6$ m. To ensure that the predetermined geometric characteristics were met, a wooden "template" was fabricated to not only position the facets at the correct distance from the centroid, but a digital inclinometer was used to set the facets to the correct tit angle. The wooden template is shown in Fig. 3. Once all the facets were installed, a water-cooled plate was positioned where the receiver aperture would be positioned and was used for the final alignment and focusing of the individual mirror facets. The water-cooled plate used for calibration is shown in Fig. 4. A summary of the geometric characteristics of the multi-facet dish assembly is shown in Table 1.

The EverBright mirror film's spectral reflectivity is 95 % on average for all light wavelengths [35,40]. Roosendaal et al. [42] determined the intercept factor for a similar multi-facet dish assembly using a novel lunar flux mapping method and calculated an intercept factor of 89.9 % for a 0.135 m × 0.135 m aperture. The results by Roosendaal et al. [42] were used to calculate the expected intercept factor for the larger 0.2 m aperture diameter used for this work (see Section 2.2). Based on the results obtained by Roosendaal et al. [36], verified by the water-cooled plate calibration work, an intercept factor of 100 % was assumed for the current work.

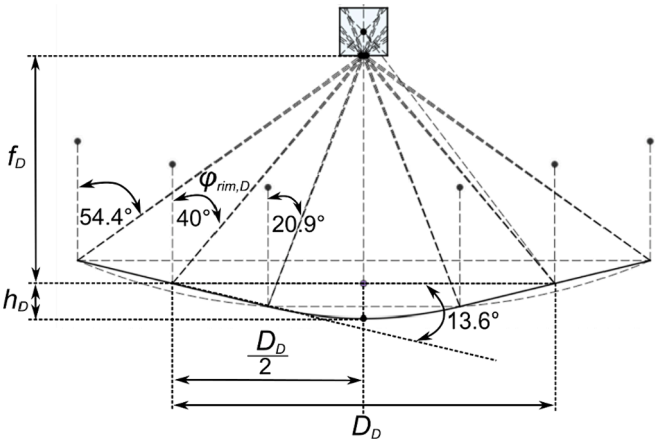

Fig. 2. Geometric dimensioning of the multi-facet dish assembly.

2.2. Solar receiver design

The solar receiver comprised a primary receiver cavity, exposed to the concentrated solar radiation, as well as a secondary zinc cavity that housed the zinc metal inventory. The as-built receiver assembly is shown in Fig. 5. A cylindrical cavity shape was selected for the receiver design based on good optical properties [17,18], and because this shape allowed for simple and cost-effective fabrication. The receiver cavity had an aperture opening of 200 mm in diameter and a cavity depth of 200 mm. The zinc cavity was radially 30 mm larger than the inner receiver cavity and this allowed for a zinc cavity volume of approximately 5.95 L. Fig. 6 illustrates all the relevant receiver design dimensions. The entire receiver assembly was fabricated from 350WA mild steel material, with the receiver vessel weighing approximately 6.7 kg, excluding the insulation material and instrumentation. The receiver cavity and zinc cavity were fully welded to one another, and the back plate of the receiver was secured in place using a flanged arrangement and sealed using a high-temperature sodium silicate-based sealant. This arrangement allowed the back plate to be unbolted when the zinc cavity had to be inspected or when the cavity was to be charged with zinc feedstock. The back plate also housed a drive shaft secured in two flanged pillow blocks, allowing the receiver to rotate freely inside the receiver support frame. The receiver support frame was, in turn, secured

Fig. 3. Facet positioning method using a wooden template and digital inclinometer.

Fig. 4. Facet calibration method using the water-cooled plate.

Table 1
Geometric design characteristics of the multi-facet dish assembly.

Parameter	Symbol	Unit	Value
Global dish diameter	D_D	m	1.6
Global rim angle	$\varphi_{rim,D}$	degrees	40
Local focal length	f_D	m	1.098
Virtual dish depth	h_d	m	0.145
Total incident reflective area	A_D	m^2	2.845

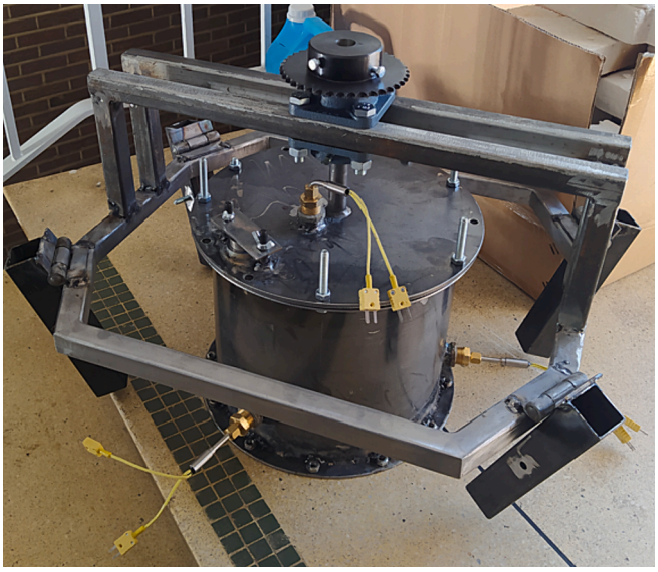

Fig. 5. As-built receiver assembly installed in the receiver support frame.

to the receiver arms to position the receiver at the focal point of the solar dish. The drive shaft was fitted to a chain and sprocket assembly, with a gear ratio of 4:1, allowing the receiver to rotate between 20 rpm and 42 rpm. The rotational system was driven by a NEMA 23 stepper motor, locally controlled from an Arduino Uno micro-controller board and a TB6600 stepper driver. A tapered steel plug was also fitted to the back plate, which was removed when the zinc inventory was fully molten, to allow the zinc metal to be drained from the zinc cavity.

Four dual-junction K-type thermocouples were used to measure the receiver cavity wall temperature and the zinc inventory temperature. Each thermocouple probe was 6 mm in diameter and housed a thermocouple junction at the tip of the probe and a second, 30 mm back. This positioning allowed for eight temperature measurements from only four openings in the zinc cavity outer wall. The thermocouples were positioned using a brass compression fitting screwed into a ½ inch socket, which was welded to the outside of the zinc cavity as well as the back plate. Three probes were positioned 50 mm up from the receiver aperture and spaced 120° apart, and the last probe was fitted through the back plate, as shown in Fig. 6. When the ports were drilled for the probes, a small divot was drilled into the outer face of the receiver cavity wall. The divot allowed the thermocouple junction positioned at the tip of the probe to make good contact with the receiver cavity wall. The second thermocouple junction is then positioned at the back of the zinc cavity and should provide a temperature representative of the entire zinc volume. TC1 to TC4 represent the thermocouple junctions at the receiver cavity wall, and TC5 to TC8 the junctions at the back of the zinc cavity.

With the thermocouple probes secured and the back plate fitted, multiple layers of ceramic fibre blanket were used to cover and insulate the receiver. Two layers were fitted to the side and the back of the receiver, resulting in an insulation thickness of 50 mm, and only a single layer of 25-mm-thick insulation was applied to the face of the receiver body. The insulation was secured in place by a combination of mechanical fasteners and Scotch 27 glass cloth electrical tape. The receiver cavity was left as untreated mild steel, of which the optical properties will be discussed in Section 3.

2.3. Data acquisition

By rotating the receiver cavity, additional complexity was added to the data logging system as no wire connections could be made to ground level as it would result in the cable being wound up around the drive system. For this reason, the entire temperature data logging system had to be mobile and rotate with the receiver. This arrangement was achieved by fitting a battery-powered temperature data logging system to the back of the receiver. The data logging system consisted of a Raspberry Pi 3B single-board computer [47] fitted with two MCC134 thermocouple data acquisition (DAQ) hats (hardware attached on top) by Measurement Computing Corporation [48]. Each of the two MCC134 DAQ hats was capable of reading four thermocouples, resulting in the required eight temperature measurements. The data logging system is shown in Fig. 7.

2.4. Solar tracking

To enable optimum solar radiation collection by the solar dish/collector, a two-axis tracking system was employed to ensure the dish was always directly facing the sun, throughout the day. The dish could be adjusted in the azimuth axis and in elevation, with both axes being operated manually. A pin-hole tracker was employed to ensure the accuracy of the manual tracking method and to confirm that the tracking error remained within 1° in each axis.

2.5. Weather data

Accurate weather data was required to evaluate the performance of the solar collector and solar receiver, as well as to serve as inputs for the analytical model. This data was collected and provided by a Tier 1 SAURAN (South African Universities Radiometric Network) [49] weather station, positioned at the top of Engineering Building 1 at the University of Pretoria. The direct normal irradiance (DNI) measurement, used as solar irradiance input for all calculations, was measured by a Kipp & Zonen CHP1 pyrheliometer, positioned on a SOLYS solar tracker. A Campbell Scientific CS215 sensor was used to measure the ambient temperature, and a R.M. Young 05103-5 sensor was used to measure the wind speed and direction. It should be noted that this weather station was not positioned directly next to the experimental setup, which would result in some discrepancies between the measured and actual wind speeds. The weather station was positioned approximately 60 m away

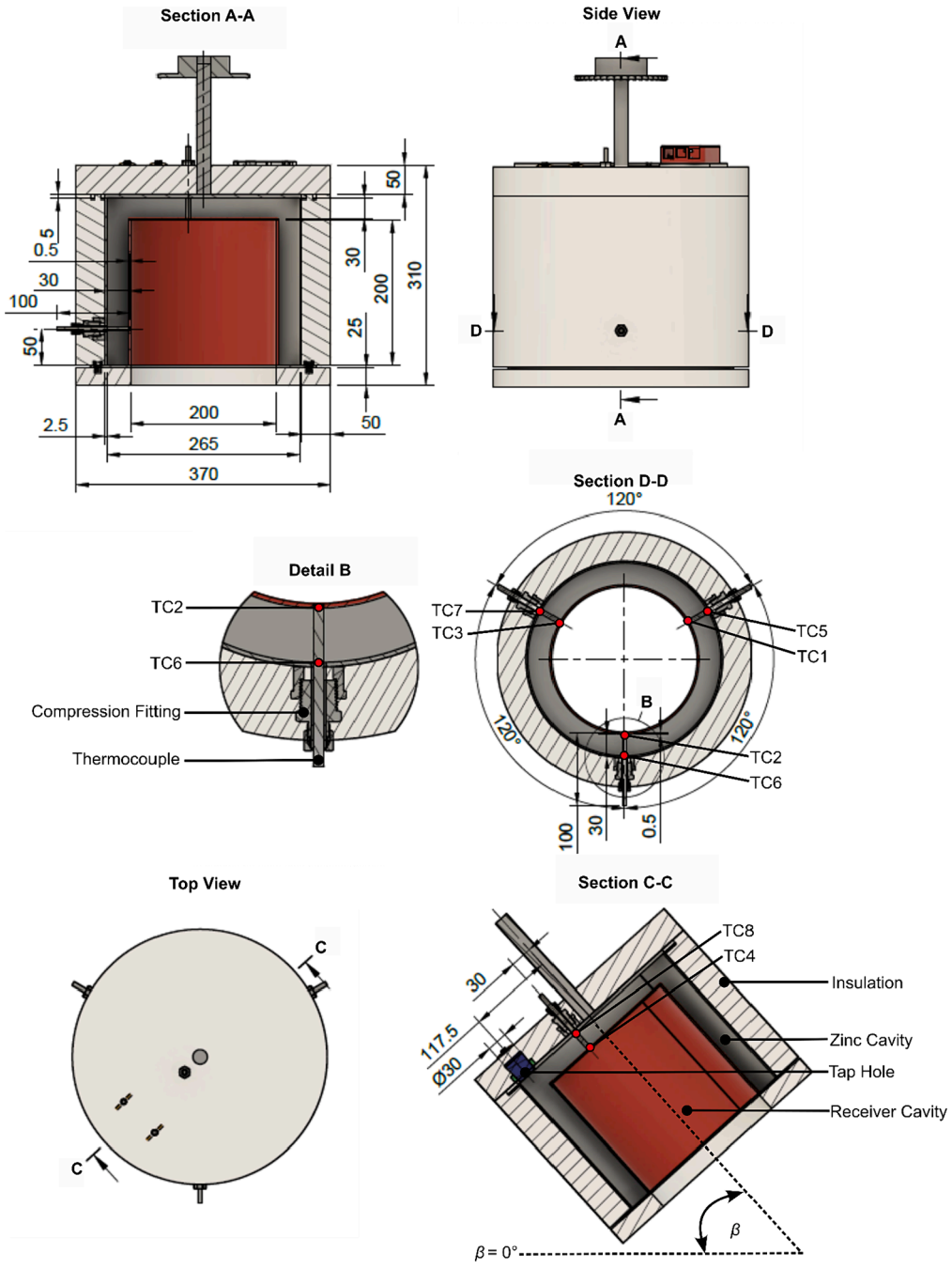

Fig. 6. Receiver design showing the major dimensions and the thermocouple positions.

from the experimental setup and approximately 30 m higher. Wind speed data collected on the same site [43] was obtained (Swanepoel, J. K., private communication, 2023) and was used to evaluate the difference in wind speed between the experimental setup and the weather station. The wind speed data of seven days were evaluated, showing that wind speeds were about 5 % higher at the experimental setup than what was measured at the weather station, however, this difference was assumed to be negligible.

2.6. Experimental method

The experimental setup was used to evaluate the solar collector and solar receiver system on five different days, to gather information over a range of environmental conditions. The elevation drive linear actuator was disconnected for easier access to the receiver frame, and a hand winch was used to tilt the dish assembly to ground level. Each experimental run started by filling the zinc cavity with solid zinc feedstock, as shown in Fig. 8. Thereafter the back plate was put in position, and the zinc cavity was sealed close. The data logging equipment was then fitted to the back of the receiver before the receiver unit was installed into the receiver frame and the drive system connected.

After the receiver had been installed, the hand winch was used to tilt back the assembly and re-connect the elevation drive. The tracking system, as well as the pin-hole tracker, was then used to get the solar dish to face the sun directly, allowing the sunlight to be focused into the centre of the receiver cavity. The vacuum behind each of the facet membranes was then drawn to concentrate the collected solar radiation to a smaller focal point into the receiver cavity. The rotation of the receiver was also activated at this time. With all of the auxiliary systems in operation, the tracking system was continuously manually adjusted to

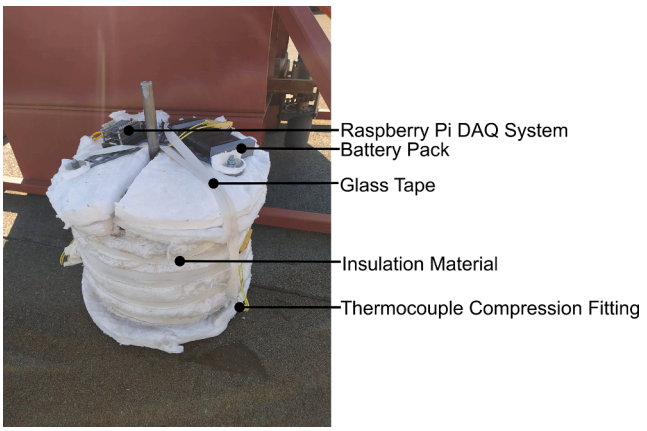

Fig. 7. The data logging system is shown fitted to the back of the receiver.

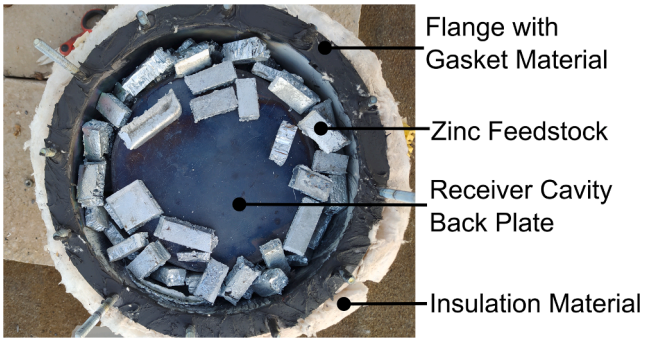

Fig. 8. Zinc cavity before heating showing the zinc feedstock and gasket material used for sealing the back plate.

keep the tracking error within 1°. Once the temperatures of the thermocouples at the zinc cavity sidewall started to rise above 420 °C (the melting point of zinc), it was assumed that the zinc inventory was fully molten and that the latent heat phase had been completed. The rotation of the receiver was then stopped, and the assembly rotated to face opposite to the sun before the assembly was lowered to the tapping position (same as the filling position). The assembly in the receiver maintenance and tapping position is shown in Fig. 9. The plug at the back of the receiver was then removed, and this allowed the molten zinc to be drained into a steel ladle coated with a ladle coating to aid in releasing the ingot from the ladle afterwards.

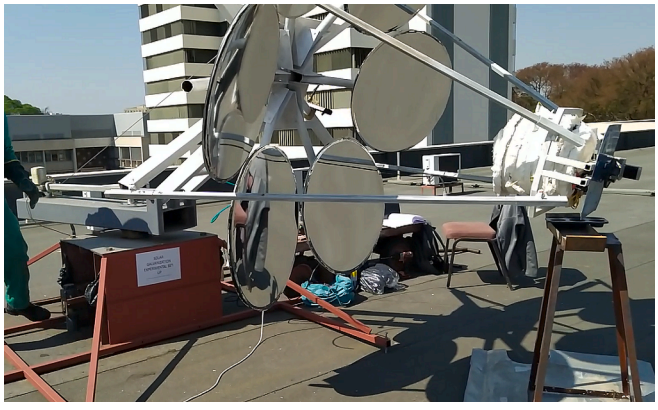

Fig. 9. Receiver charging and discharging position with the whole assembly lowered to ground level for easier access (orientated to face away from the sun).

3. Analytical model

In this section, the theory and assumptions used to compile the analytical model are described and discussed. The different heat loss mechanisms are evaluated and the methodology and theory used for each are described in sufficient detail. Also in this section, the method for calculating the heat loss or heat gain in the zinc inventory is described. The thermal analysis model was developed in the Python programming language [50] to calculate the first-law thermal efficiency (at each timestep) for the receiver, as shown in Eq. (1). The model considered solar data as energy input as well as the heat loss associated with the receiver design, orientational movement, and environmental conditions. The model results were then validated against the experimental results.

$$\eta_{th,rec} = \frac{\dot{Q}_{net}}{\dot{Q}_{ap,in}} \tag{1}$$

A schematic of the receiver and the heat losses are shown in Fig. 10. The heat loss mechanisms from the receiver consists of conduction, convection, and radiation. The net heat transfer rate available in the zinc cavity is calculated using Eq. (2). Constant c is the heat transfer efficiency constant that will be discussed in greater detail in the results section but is used to correct for the fill density in the zinc feedstock and for contact between the receiver wall and the zinc. Air gaps in the zinc feedstock negatively affect the heat transfer between the receiver cavity wall and the zinc.

$$\dot{Q}_{net} = c \bullet \dot{Q}_{wall} = c \bullet (\dot{Q}_{ap,in} - (\dot{Q}_{cond,loss} + \dot{Q}_{conv,loss} + \dot{Q}_{rad,loss})) \tag{2}$$

The useful solar heat supplied at the receiver aperture is expressed in Eq. (3) [51]. This equation considers the DNI reaching the solar reflector surface area (A_D) and the reflector efficiency (η_D).

$$\dot{Q}_{ap,in} = I \bullet A_D \bullet \eta_D \tag{3}$$

The reflector efficiency shown in Eq. (4), depends on the geometry, manufacturing process, imperfections, mirror soiling, reflector material, and optical properties [51].

$$\eta_D = \Gamma \bullet f_s \bullet \rho_D \tag{4}$$

3.1. Conduction heat loss

At elevated temperatures, conduction heat loss from the receiver walls represents a small fraction of the total receiver heat losses, if sufficient insulation is applied [15,52]. The insulation thickness is

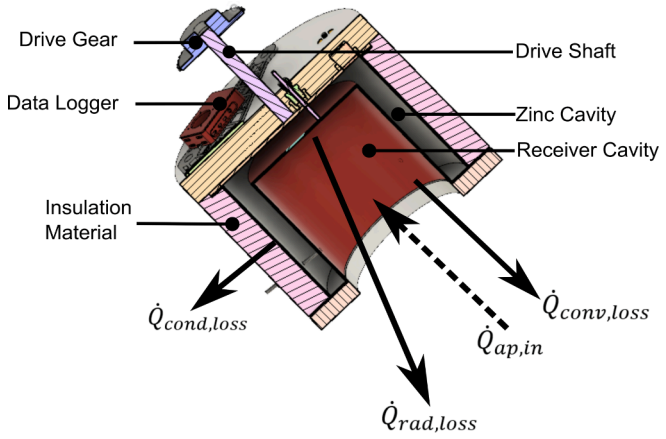

Fig. 10. Schematic of heat loss mechanisms from the open-cavity receiver exposed to the environment. Note that the zinc is in contact with the open-cavity receiver walls on the inside as well as with the insulation on the outside, and the whole setup rotates around the drive shaft.

typically specified in such a manner as to limit the conductive heat losses while limiting the shading factor of the receiver. Because of the use of the multi-facet dish design, the shading factor was not of real concern and was specified as $f_s = 1$. For this receiver design, ceramic fibre blanket insulation material was selected to be used as receiver insulation based on the material's low thermal conductivity, flexibility, and availability. The ceramic fibre blanket has a thermal conductivity of 0.11 W/mK at 673 K [53]. The conduction heat loss from the receiver insulation is calculated as per Eq. (5), assuming that the average zinc temperature is equal to the average wall temperature.

$$\dot{Q}_{cond,loss} = \frac{(T_{Zn,ave} - T_\infty)}{R_{tot}} \tag{5}$$

The combined thermal resistance (R_{tot}) of the cylindrical receiver system can be calculated by Eq. (6), with R_{ins} and R_{conv} the insulation and convection resistances, respectively [13].

$$R_{tot} = R_{ins} + R_{conv} = \frac{\ln\left(\frac{r_{o,ins}}{r_{i,ins}}\right)}{2\pi L_{rec} k_{ins}} + \frac{1}{2\pi r_{o,ins} L_{rec} h_o} \tag{6}$$

The convection heat transfer coefficient (h_o) represents a combination of natural and forced convection at the outer surface of the receiver insulation material. Forced convection will be dependent on the wind speed and angle of attack. Cross-flow over the receiver was assumed for all scenarios. Heat loss from the back of the receiver was neglected as it was fitted with an additional insulation layer and was shielded by a sun shield installed to protect the data logger. Conduction heat losses from the drive shaft were also neglected due to the relatively small area of this component. To determine the convection coefficient, the average Nusselt number ($Nu_{D,forc}$) for forced convection over a cylinder in a cross-flow wind was evaluated using Eq. (7) and Eq. (8) [13].

$$h_o = \frac{Nu_{D,forc} k_{ins}}{D_{ins}} \tag{7}$$

$$Nu_{D,forc} = \frac{h_0 D_{ins}}{k_{ins}} = C Re_{D,ins}^m Pr^{1/3} \tag{8}$$

Constants C and m for cylinders in cross-flow used for Eq. (8) can be found in [13], based on the calculated Reynolds numbers ($Re_{D,ins}$) as defined by Eq. (9) [13].

$$Re_{D,ins} = \frac{\rho_{air} V_{wind} D_{ins}}{\mu_{air}} \tag{9}$$

The natural convection Nusselt number for a cylindrical body is calculated as per Eq. (10) [13], valid for $Ra_{D,ins} \leq 10^{12}$, where $Ra_{D,ins}$ is the Rayleigh number ($Ra_{D,ins} = Gr_L Pr$) and Pr the Prandtl number.

$$Nu_{D,nat} = \left(0.6 + \frac{0.387 Ra_{D,ins}^{\frac{1}{6}}}{\left(1 + \left(\frac{0.559}{Pr}\right)^{\frac{9}{16}}\right)^{\frac{8}{27}}}\right)^2 \tag{10}$$

To determine the state of natural and forced convection, the following check can be done, as shown in Table 2.

Table 2
Check for combining natural and forced convection [13].

Check	Outcome
$\frac{Gr_L}{Re_L^2} < 0.1$	Natural convection is negligible
$\frac{Gr_L}{Re_L^2} > 10$	Forced convection is negligible
$0.1 \leq \frac{Gr_L}{Re_L^2} \leq 10$	Natural and forced convection need to be combined

The Grashof number is calculated using Eq. (11), with all the air properties calculated at the average temperature between the exposed insulation surface and the ambient conditions.

$$Gr_L = \frac{g\beta_v (T_{s,ins} - T_\infty) L_{rec}^3}{\nu_{air}^2} \tag{11}$$

To calculate the combined Nusselt number for the natural and forced convection, Eq. (12) is employed with $n = 4$ for transverse flows involving cylindrical bodies [13].

$$Nu_D^n = Nu_{D,forc}^n + Nu_{D,nat}^n \tag{12}$$

3.2. Convection heat loss

The convection heat loss from the receiver's cavity is calculated as per Eq. (13), and the internal convection heat transfer coefficient, h_{in}, is shown in Eq. (14).

$$\dot{Q}_{conv,loss} = A_{cav} h_{in} (T_{cav} - T_\infty) \tag{13}$$

$$h_{in} = Nu \frac{k}{D_{ap}} \tag{14}$$

The Nusselt number (Nu) is dependent on the wind conditions. The wind speed and direction will determine whether or not natural convection, forced convection, or a combination of both take place inside the receiver cavity.

For wind speeds below 1.5 m/s, the Nusselt number for natural convection is calculated using an equation proposed by Stine and McDonald [22]. This equation is shown in Eq. (15), with $P(\theta)$ a function of the receiver tilt angle and l_c the characteristic length represented by the receiver aperture-cavity radius ratio [22].

$$Nu_{cav,nat} = 0.78 P(\theta) l_c^{1.75} (Gr \bullet Pr)^{0.25} \tag{15}$$

To calculate the Nusselt number for natural convection, for wind speeds between 1.5 m/s and 5 m/s, a correlation proposed by Wu et al. [31] was considered and is shown in Eq. (16).

$$Nu_{cav,nat} = 0.00106 Gr^{0.149} (2 + cos\beta)^{7.228} (1 + \varepsilon_{cav})^{-0.0849} \left(\frac{d}{D_i}\right)^{1.466} \tag{16}$$

With regard to forced convection, a Nusselt number correlation proposed by Reddy et al. [27] was considered for all wind speeds below 5 m/s (see Eq. (17)). β represents the receiver inclination angle (refer to Fig. 6) and φ the incident angle of the wind, with 0° representing a side-on wind, 90° a head-on wind, and −90° a back-on wind, relative to the receiver aperture. The Grashof and Reynolds numbers are calculated using Eq. (18) and Eq. (19), respectively. It should be noted, however, that Reddy et al. [27] evaluated a modified hemispherical cavity receiver, whereas this study evaluated a cylindrical cavity receiver.

$$Nu_{cav,forc} = p(1 + cos\beta)^q (3 + sin\varphi + sin2\varphi + sin3\varphi)^r \left(\frac{d}{D_i}\right)^s \left(\frac{Gr}{Re^2}\right)^t \tag{17}$$

$$Gr = \frac{g\beta_v (T_{cav} - T_\infty) D_{ap}^3}{\nu_{air}^2} \tag{18}$$

$$Re = \frac{\rho_{air} V_{wind} D_{ap}}{\mu_{air}} \tag{19}$$

For wind speeds in excess of 5 m/s, equations proposed by Bergman et al. [13] were utilized for natural convection (see Eq. (20)) and forced convection (see Eq. (21)).

$$Nu_{cav,nat} = 0.52 (Gr \bullet Pr)^{0.2} \tag{20}$$

$$Nu_{cav,forc} = 0.68 Re^{0.5} Pr^{0.333} \tag{21}$$

The procedure for defining the convection state is by evaluating the

$\left(\frac{Gr}{Re^2}\right)$ relationship, as shown in the conduction heat loss discussion. As the convection heat loss is calculated for a cavity, not cross-flow over a cylinder, this relationship will not be a precise estimation [13]. This method was described in detail in the conduction heat loss section above and summarized in Table 2.

All air properties were calculated based on the bulk mean temperature (T_{bulk}) as shown in Eq. (22). An average cavity wall temperature was assumed for the cavity and this was also the approach employed by the Nusselt number correlations [22,26]. In the model, the cavity wall temperature is assumed to be the same as the zinc temperature ($T_{Zn,ave}$).

$$T_{bulk} = \frac{T_\infty + T_{Zn,ave}}{2} \tag{22}$$

3.3. Radiation heat loss

At elevated temperatures, radiation heat loss contributes a significant fraction of the total heat loss from the receiver [15,54]. As opposed to the other two heat loss mechanisms, radiation heat loss remains relatively constant throughout the day once a steady-state temperature has been reached inside the receiver [15]. The total radiation heat loss from a receiver cavity is the result of emission and reflection from the inside of the cavity [15,51,54].

Radiation heat loss due to emission ($\dot{Q}_{rad,em}$) from inside the cavity is calculated as per Eq. (23) [51], with ε_{eff} the effective emissivity based on the cavity emissivity (ε_{cav}) and the aperture surface area (A_{ap}) to cavity surface area (A_{cav}) ratio, as calculated in Eq. (24). The cavity emissivity (ε_{cav}) is a function of temperature as shown in Eq. (25) [55].

$$\dot{Q}_{rad,em} = \varepsilon_{eff}\sigma A_{ap}(T_{cav}^4 - T_\infty^4) \tag{23}$$

$$\varepsilon_{eff} = \frac{\varepsilon_{cav}}{1-(1-\varepsilon_{cav})\left(1-\frac{A_{ap}}{A_{cav}}\right)} \tag{24}$$

$$\varepsilon_{cav} = 0.28, \text{ for } T < 380^\circ C;$$

$$\varepsilon_{cav} = 0.00293T - 0.833, \text{ for } 380^\circ C \le T < 520^\circ C;$$

$$\varepsilon_{cav} = 0.69, \text{ for } T \ge 520^\circ C \tag{25}$$

To calculate the radiation heat loss as a result of reflection ($\dot{Q}_{rad,ref}$) from inside the receiver, through the aperture, Eq. (26) is used. With α_{eff} the effective absorptance, calculated as per Eq. (27) [51], and $\dot{Q}_{ap,in}$ the total solar energy supplied to the receiver aperture. The cavity absorptance (α_{cav}) for this study was assumed to be 0.52 [56].

$$\dot{Q}_{rad,ref} = (1-\alpha_{eff})\dot{Q}_{ap,in} \tag{26}$$

$$\alpha_{eff} = \frac{\alpha_{cav}}{1-(1-\alpha_{cav})\left(1-\frac{A_{ap}}{A_{cav}}\right)} \tag{27}$$

The total radiation heat loss ($\dot{Q}_{rad,loss}$) from the receiver was calculated as the sum of the radiation losses as a result of emitted and reflected radiation as per Eq. (28).

$$\dot{Q}_{rad,loss} = \dot{Q}_{rad,em} + \dot{Q}_{rad,ref} \tag{28}$$

3.4. Heat gain calculation

With the heat input and all the heat losses accounted for, the heat gain of the zinc metal inventory can be calculated to determine at which time step the zinc inventory will be fully molten. This is achieved by using three stages, starting with the sensible heating stage, during which the entire batch is still solid, followed by a transition phase known as the latent phase, and then a second sensible heating phase, during which the molten material (liquid) is heated further. During the liquid heating phase, the zinc material is heated beyond the melting point to aid in the successful tapping of the material from the receiver.

During the solid heating phase, Eq. (29) applies [13]. T_{t-1} represents the temperature of the zinc batch at the beginning of the time step (Δt = 1 min), and is used together with the available heat during the time step ($Q_{net} = \dot{Q}_{net} \times 60$), to calculate the zinc cavity temperature, T_t, at the end of the time step. This process is repeated until the melting point of zinc is reached. During the solid heating phase, both the zinc batch mass and the mass of the receiver steel are considered. To incorporate the mass of both the zinc and receiver, an average of the resultant specific heat capacity (c_p) is calculated at the system temperature for each time step.

$$\dot{Q}_{net} = (m_{zn} + m_{steel}) \bullet \frac{(c_{p_{solid-Zn}} + c_{p_{steel}})}{2} \bullet (T_t - T_{t-1})/60 \tag{29}$$

Once the melting point is reached, the latent heating phase represented by Eq. (30) [13], comes into effect. This phase makes use of the latent heat of fusion (λ_{zn}) to calculate the amount of heat added to the zinc material. For every time step in this phase, Eq. (31) is in effect during which the mass of zinc that is already molten ($m_{zn,liquid(t-1)}$) is added to the mass of molten material formed during that time step. This process is repeated until the entire batch of zinc is in the liquid state. For the latent heating phase, only the mass of the zinc batch is considered, as the steel temperature would show little to no temperature change during this phase.

$$\frac{\lambda_{zn}}{60} = \frac{\dot{Q}_{net}}{m_{zn}} \tag{30}$$

$$m_{zn,liquid(t)} = m_{zn,liquid(t-1)} + \left(\frac{60 \bullet \dot{Q}_{net}}{\lambda_{zn}}\right) \tag{31}$$

With the entire batch of zinc in the liquid state, the liquid heating occurs, as per Eq. (32) [13]. This process will continue to a specified cut-off temperature. An additional 20 K was added to the zinc melting temperature before it was removed from the heat source to be tapped. The additional heating was aimed at limiting the amount of zinc inventory that solidifies in the receiver during the tapping procedure as a result of heat losses. During the liquid heating phase, the mass of both the zinc batch and receiver steel is again considered, as both would require energy to increase in temperature.

$$\dot{Q}_{net} = (m_{zn} + m_{steel}) \bullet \frac{(c_{p_{liquid-Zn}} + c_{p_{steel}})}{2} \bullet (T_t - T_{t-1})/60 \tag{32}$$

4. Results

In this section, five experimental test runs that were executed as part of this study are discussed in great detail to describe the unique environmental conditions that were associated with each run (a summary can be found in Appendix A). The detailed discussions describe the lessons learned and conclusions drawn from each experimental run. The results produced by the analytical model are included in this section, together with a detailed description of how the analytical model compares with the experimental results. A discussion follows on the efficiency of the system and the influence that the different environmental conditions have.

4.1. Experimental results

Each of the five experimental tests was executed as per the discussed experimental method (see Table 3).

4.1.1. Experiment 1 & 2

The first experimental run started at 13:36 on the 26th of July 2022. The late start resulted in the DNI starting to decrease steadily, as shown

Table 3
Molten zinc recovery by mass.

Test	Zinc mass [kg]	Mass drained [kg]	Mass remaining [kg]	Recovery [%]
1	10.01	0	10.01	0
2	10.01	3.05	6.95	30.52
3	16.96	12.46	4.50	73.47
4	14.52	10.25	4.24	70.82
5	10.01	2.52	7.54	25.04

in Fig. 11, which ultimately resulted in the zinc not reaching the melting temperature of 420 °C. An average DNI of 688 W/m^2 and wind speed of 2.01 m/s was recorded during Experiment 1. TC6 and TC7 represent the thermocouples inside the zinc material, as illustrated in Fig. 6. TC8 represents the temperature of the zinc cavity at the back of the receiver. As the zinc feedstock settles to the front of the receiver due to gravity and receiver orientation, it can be assumed that the temperature represents the air pocket temperature inside the zinc cavity. This air pocket is likely why TC8 measures lower temperatures in all the experiments because it is not in constant contact with zinc metal. TC2 to TC4 represent the temperatures of the receiver cavity, and the position of each is shown in Fig. 6. TC1 and TC5 were found to be faulty and assumed to have been damaged during installation. The irregular noise in the TC4 data is also most likely due to a damaged thermocouple, as it does not follow any of the other trends. The missing data around the 1-hour mark resulted from a data logger failure, but after a restart, the data logging continued. The same receiver was used for Experiments 1 to 4, and a new receiver was used for Experiment 5. This decision resulted in some interesting findings, which will be discussed below.

Experiment 2 started at 10:12 on the 8th of August 2022 and used the same receiver and inventory as Experiment 1. It can be noticed that the receiver cavity temperatures (TC2 to TC4) sharply increased while the zinc temperatures (TC6 to TC8) increased more slowly, as shown in Fig. 12. A better average DNI of 792 W/m^2 was recorded together with a slightly higher average wind speed of 2.68 m/s, when compared to Experiment 1. As the zinc temperature approaches the melting temperature, the receiver and zinc temperature get closer to one another, as expected, due to material softening and settling around the thermocouples and allowing for better heat transfer from the receiver cavity to the zinc. The limited deviation between the receiver temperature measurements points to a uniform receiver cavity temperature, which translates to the uniform heating of the zinc inventory. The control philosophy was to heat the receiver until temperature measurements above the melting point of zinc were observed, pointing to the latent heat phase being completed, and the zinc inventory being fully molten. This was not completely the case, and will be discussed in the analytical model results section.

During Experiments 1 and 2, the face of the receiver was not protected with insulation material, resulting in excess heat loss. Not only did the exposed face result in a higher heat input required to melt down the zinc feedstock, but the enlarged exposed surface and the resultant increased heat losses could also cause the molten material to solidify again before it could be drained from the receiver. The increased heat loss, together with the time taken during the tapping procedure due to initial inexperience, is most likely why only 30.52 % of the zinc inventory could be drained from the receiver in the molten form, as listed in Table 3. The increased heat loss was accounted for in the analytical model by adding additional convection heat loss from the faceplate of the receiver, as shown in Eq. (33). The additional convection heat loss was calculated in the same manner as described in Section 3.2, with the exception of the gravitational constant which was calculated as per Eq. (34) [13] to account for the buoyancy of the air in the Grashof number. The ratio between the surface area of the faceplate and the circumference of the faceplate represents the characteristic length used for the faceplate calculations.

$$\dot{Q}_{conv,loss} = (A_{cav} h_{in} (T_{cav} - T_\infty)) + (A_{faceplate} h_{faceplate} (T_{cav} - T_\infty)) \tag{33}$$

$$g_{faceplate} = g\cos(90^\circ - \beta),\ for\ 0^\circ \leq (90^\circ - \beta) \leq 60^\circ$$

$$g_{faceplate} = g,\ for\ (90^\circ - \beta) > 60^\circ \tag{34}$$

4.1.2. Experiment 3 & 4

For Experiment 3, starting at 09:21 on the 16th of August, additional insulation was added to the face plate of the receiver, as illustrated in Fig. 6 and Fig. 10, with the aim of reducing the heat loss from this area of the receiver. The results of Experiment 3 are shown in Fig. 13. During Experiment 3 the highest average DNI of 910 W/m^2, out of the five experiments, were recorded together with an average wind speed of 2.14 m/s. It is assumed that the remaining inventory from Experiment 2 settled and solidified around the thermocouples towards the face side of the receiver. This assumption is based on a visual inspection of when the new zinc feedstock was added and the comparable temperatures between the receiver cavity temperatures and that of the zinc inventory, pointing to fewer voids in the feedstock. This packing arrangement improved the heat transfer significantly and reduced the heat input required to get the inventory to the molten state. The reduced heat loss from the receiver and the improved heat transfer between the receiver cavity and the zinc resulted in a steady and uniform heat-up of the complete system. TC4 follows the same trend at the beginning, pointing

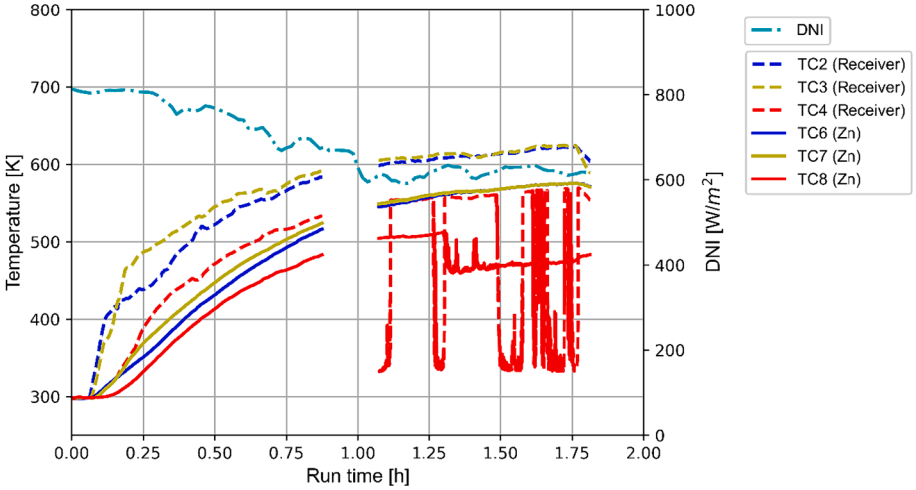

Fig. 11. Receiver temperatures - Experiment 1 on the 26th of July 2022.

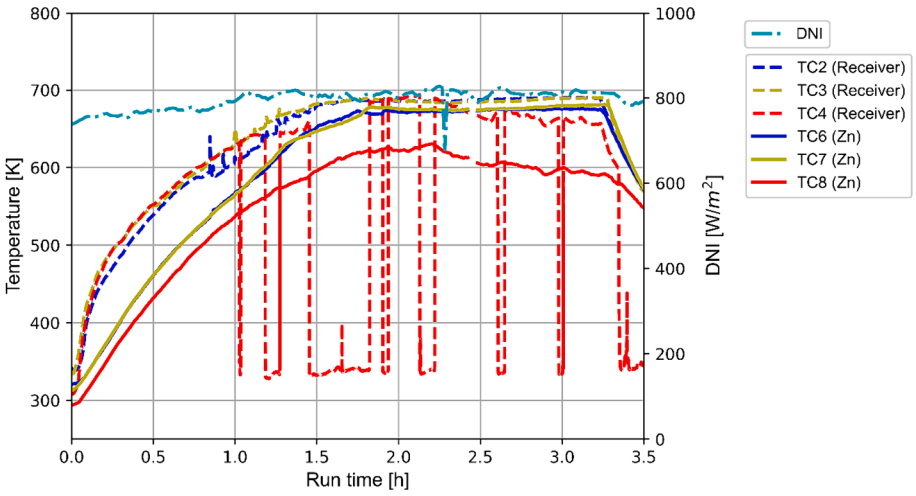

Fig. 12. Receiver temperatures - Experiment 2 on the 4th of August 2022.

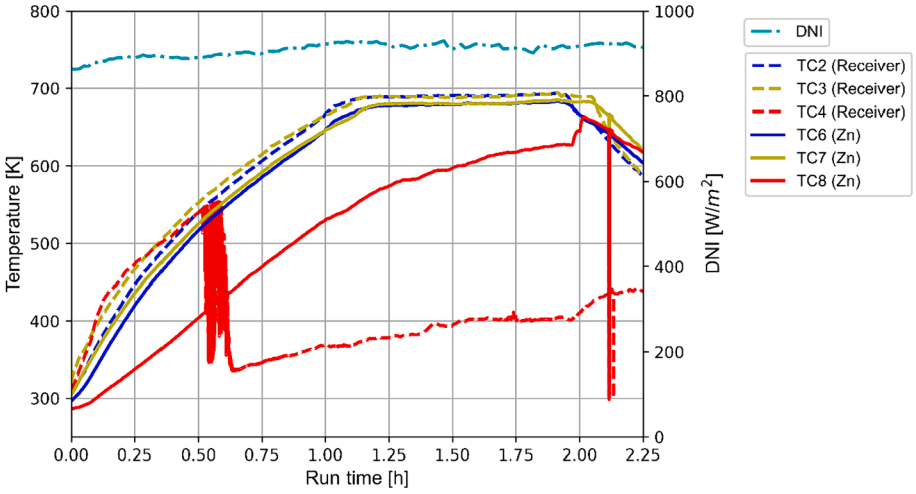

Fig. 13. Receiver temperatures - Experiment 3 on the 16th of August 2022.

to a uniformly heated cavity, but then starts to malfunction around the half-hour mark. TC8 is likely not in contact with any process material and is, as a result, only measuring the air pocket temperature in the back of the zinc cavity. The uniform heat-up and stopping the experiment at the correct time to drain the molten inventory resulted in 73.47 % of the zinc inventory being drained from the receiver in its molten state. The inventory that was not drained is believed to be a result of the high thermal conductivity of zinc and the time it took to drain the inventory,

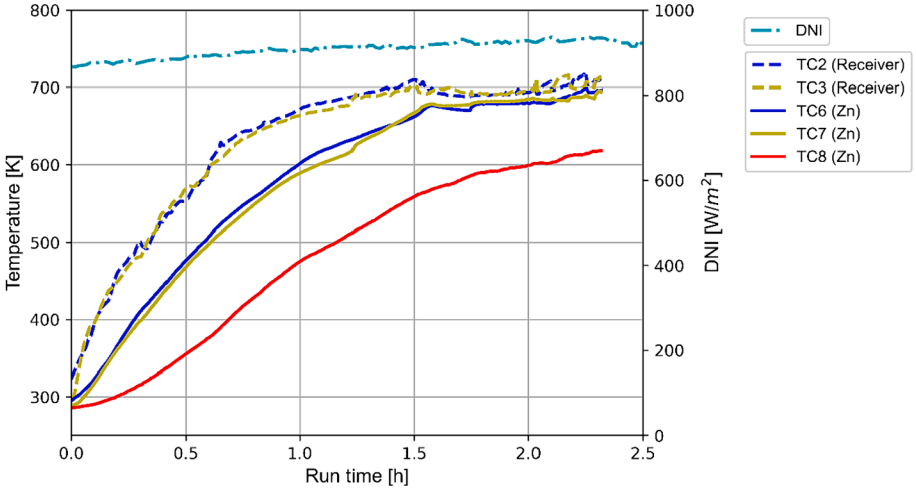

Fig. 14. Receiver temperatures - Experiment 4 on the 21st of August 2022.

causing some material to solidify in the receiver, as all other indications pointed to the complete inventory being melted down.

Experiment 4 started at 09:11 on the 21st of August 2022, containing some solidified inventory from Experiment 3, but a visual inspection revealed that the material from Experiment 3 was drained to below the thermocouple position. Additional zinc feedstock was added to the receiver, adding voids in the inventory and is most likely the reason why a significant temperature difference between the receiver cavity temperature and zinc temperatures is noticed, as shown in Fig. 14. Even though good solar irradiance was recorded on this day (908 W/m^2), similar to Experiment 3, much higher wind speeds (5.26 m/s) were recorded which drastically increased heat loss from the receiver. The influence of the wind speed will be discussed in greater detail in the analytical model results section. The higher heat loss resulted in less zinc being tapped from the receiver (70.82 %) even though this receiver was kept at the focal point of the parabolic dish for about 30 min longer than in Experiment 3. TC4 is believed to have completely malfunctioned during this experiment; therefore, the results are not reflected in Fig. 14. TC 8 is again believed not to have been in contact with any process material.

4.1.3. Experiment 5

The last experiment, Experiment 5, took place on the 5th of September 2022, and the test was initiated at 08:36. This test made use of a new receiver vessel with a fresh batch of zinc feedstock. This entailed a completely new fabricated receiver fitted with new insulation material and a new set of thermocouples. An average DNI of 835 W/m^2 was recorded together with the lowest average wind speed, out of the 5 experiments, of 0.95 m/s. Similar trends to Experiment 1 were noticed and are shown in Fig. 15. All eight thermocouples were functional and pointed to uniform heating in the zinc feedstock, even though the receiver cavity temperatures did point to some irregularities. These irregularities can be a result of how and where the zinc feedstock made contact with the receiver cavity wall, utilizing heat more efficiently at some positions and less at others, resulting in localized heating. Localized heating around 2.4 h into the test (at thermocouple TC2) resulted in the zinc inventory being drained prematurely and resulted in only 25.04 % of the inventory being recovered from the receiver in the molten form. This action was a result of the experimental procedure, which dictated that if temperatures above 720 K were recorded after the latent heating phase, the molten material had to be tapped from the receiver. During this experiment, there were also some operational issues with the multi-facet dishes, during which three of the facets started to lose the vacuum behind the reflective membrane. These facets had to be replaced during the test. At 20 min into the test, the first facet started to show signs of a leak, followed by a second around the 40-minute mark. An attempt was made to repair the leaking facets in situ, but in failing to repair them, these two facets were replaced with new facets after an hour and 15 min. A third started to leak around an hour and a half into the test and was replaced with a new facet just before the two-hour mark. The test was then completed without any leaking facets.

Fig. 16 shows the typical product obtained from the experimental process. The zinc was tapped into a rectangular ladle and a cupcake mould, for a more manageable form factor.

4.2. Analytical results

A Python model was developed, based on the literature discussed in the analytical model section, and is used to calculate the heat balance, considering the optical and design properties of both the receiver and the parabolic dish collector. The heat balance is based on the solar irradiance, ambient temperature, receiver orientation, wind speed, and wind angle obtained from the historical weather data.

The results from the analytical model were compared with the experimental results, not only to validate the model but also to refine user input assumptions made during the development of the model. In an attempt to account for the uncertainty related to the heat transfer between the solid zinc particles and between the receiver wall and zinc particles, a heat transfer efficiency constant, c, was included in the

Fig. 16. Casted zinc ingots.

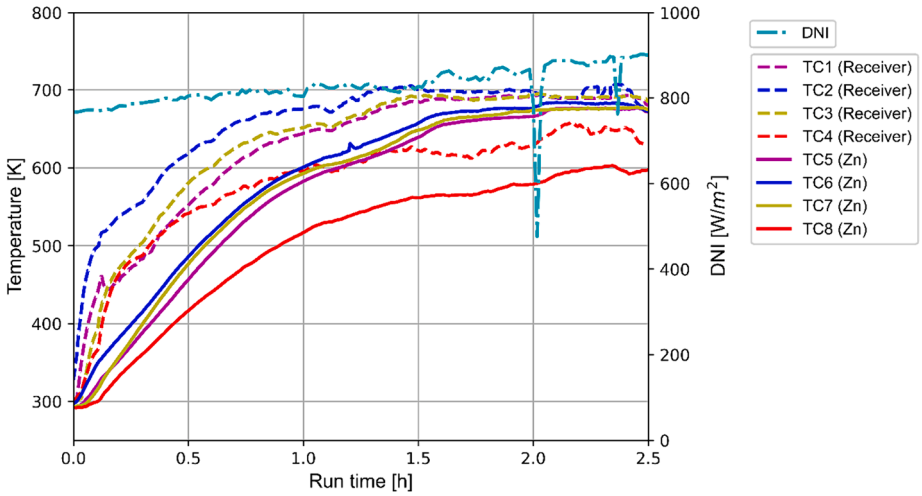

Fig. 15. Receiver temperatures - Experiment 5 on the 5th of September 2022.

model. This heat transfer efficiency constant will be unique to each test run as no packing structures will be the same in how and where the zinc feedstock makes contact internally and with the cavity wall.

The results obtained from the analytical model were compared with the experimental results, and are shown in Figs. 17–21. One of the first observations made is that the zinc melted at temperatures slightly lower than the theoretical melting point (approximately 10 °C lower), and this is observed in all the experiments where the melting point had been reached (Figs. 18–21). This discrepancy is most likely due to the measurement resolution of the thermocouples used (±2°C) together with material impurities in the zinc that resulted in a slightly lower melting point.

4.2.1. Comparison with Experiment 1

In Fig. 17, the results for the first experiment are shown together with the output of the analytical model using the historical weather data for the test duration. The first experimental run served as a training exercise, and the face of the receiver cavity was exposed to environmental conditions. The temperature difference between the receiver and the zinc is believed to be a result of the voids within the solid zinc feedstock that result in less-than-ideal heat transfer. The feedstock size also limits the volume of zinc material that fits in the zinc cavity – in this instance, only 47 % of the zinc cavity was occupied by zinc material, with the rest taken up by air voids. The predictive analytical model assumes complete surface contact between the receiver cavity wall and the zinc feedstock, with no voids in the feedstock if $c = 1$. In order to match the predictive model to the zinc temperatures obtained in Experiment 1, a heat transfer efficiency constant of $c = 0.5$ was required.

4.2.2. Comparison with Experiment 2

Experiment 2 is compared to the analytical model in Fig. 18. This experiment was executed using the same inventory left over from Experiment 1 and the same receiver setup, with the main difference being the environmental conditions. Experiment 2 was started much earlier during the day, and as a result, the receiver was exposed to much higher DNI intensities. The sun's position was also different from Experiment 1 (see Appendix A), resulting in a lower receiver tilt angle, ensuring more movement in the zinc feedstock and potentially improving heat transfer. As with Experiment 1, a significant discrepancy between the receiver temperature and that of the zinc is noticed until the melting temperature of zinc is reached, and the melting material ensures sufficient contact with the receiver cavity wall. This phenomenon is expected due to an improved heat transfer as the air voids between the zinc particles are reduced and better surface contact is made with the heated surface. In order to match the experimental zinc temperature to that of the predictive model, a heat transfer efficiency constant of $c = 0.4$ was required. The lower heat transfer efficiency constant than what was required for Experiment 1 can be due to the higher wind speeds observed during this experiment. The higher wind speeds could exaggerate the heat losses from the receiver due to the exposed receiver face. The analytical model also explains why only 30.5 % of the zinc feedstock was tapped in the molten form. As demonstrated by the analytical model results, the latent heating phase had not been completed yet, and the receiver was drained prematurely during the experiment. If the latent phase had finished, an increase in the temperature would have been noticeable in the model curve (see Fig. 19, for example).

4.2.3. Comparison with Experiment 3

Experiment 3 (see Fig. 19) was the only one of the five experiments where the thermocouples were entirely covered by solid material. The results from Experiment 2 showed that the melting point was reached, and as a result, most of the inventory softened and settled to the front of the zinc cavity. The material that remained in the zinc cavity after Experiment 2 solidified, but this time with much fewer voids and in good contact with the receiver cavity wall. Another change to Experiment 3 was the addition of insulation material to the face plate of the receiver in an attempt to reduce the heat losses from this area. In Fig. 19, the results for Experiment 3 are shown, and it is clear that the receiver wall and zinc temperatures follow the same trend as opposed to the other four experiments. The analytical model also accurately predicts these temperatures. Because the zinc and cavity temperatures follow the same trend, the model prediction is much more representative of the zinc material temperatures, which was the intent of the analytical model. Experiment 3 illustrates the most ideal conditions out of all the experiments from the analytical model point of view. The approximately full zinc cavity, with limited voids resulting from Experiment 2, allows for the heat transfer mechanisms assumed in the analytical model. The analytical model assumes a solid zinc inventory which ensures good contact with the receiver cavity wall. This assumption is most closely reproduced in Experiment 3, and the fact that the model so closely predicts the zinc temperatures provides confidence in the accuracy of the analytical model. A heat transfer efficiency constant of $c = 1$ was required, which alludes to no correction required to match the predictive model to the experimental results obtained for Experiment 3.

Fig. 19 shows the reason for the good recovery of molten material from the receiver (see Table 3) during the tapping procedure of Experiment 3, which was that the latent heating phase was just about completed when the experiment was stopped to tap the zinc. This is

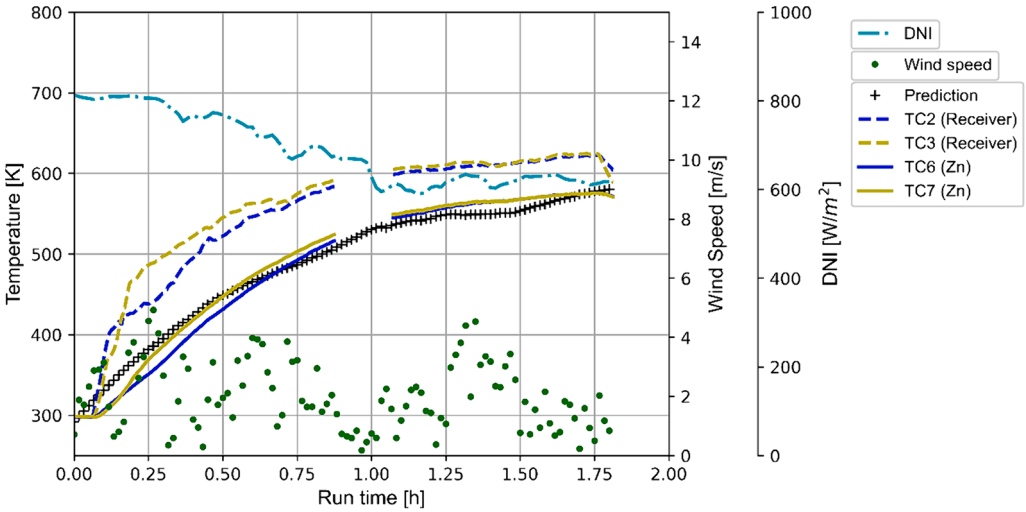

Fig. 17. Experiment 1 compared to the analytical model prediction based on historical weather data.

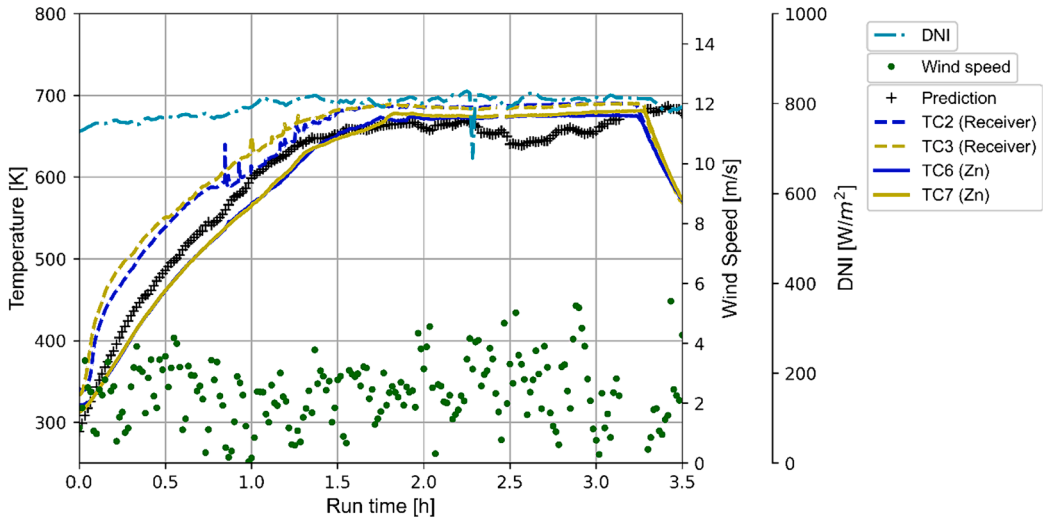

Fig. 18. Experiment 2 compared to the analytical model prediction based on historical weather data.

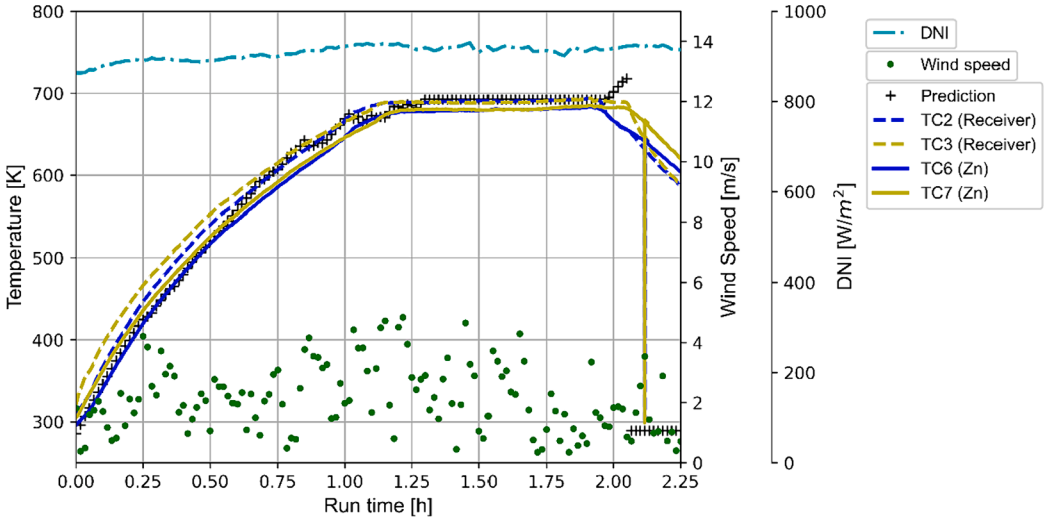

Fig. 19. Experiment 3 compared to the analytical model prediction based on historical weather data.

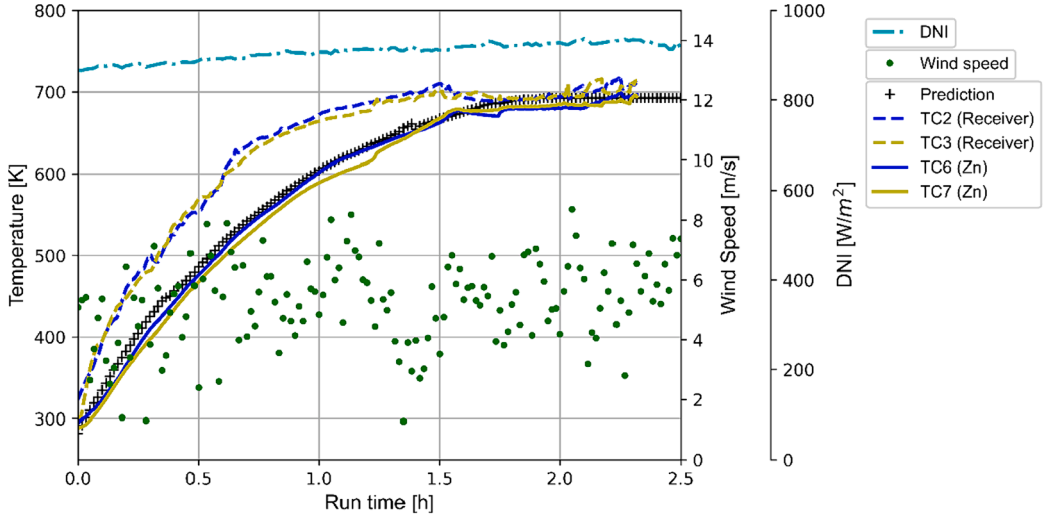

Fig. 20. Experiment 4 compared to the analytical model prediction based on historical weather data.

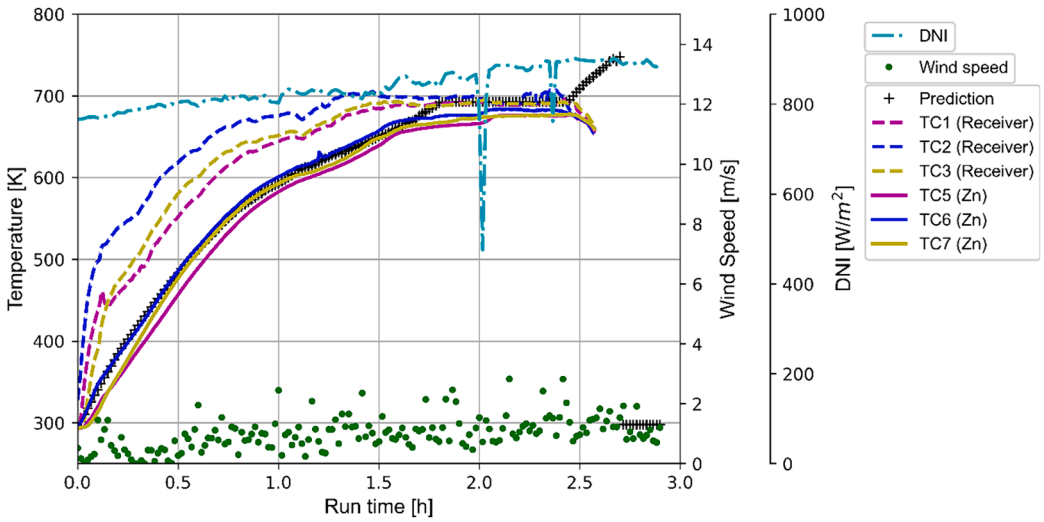

Fig. 21. Experiment 5 compared to the analytical model prediction based on historical weather data.

shown by the sharp increase in the predicted temperature after the latent heating phase, which coincides with when the receiver was removed from the heat source to be tapped.

4.2.4. Comparison with Experiment 4

Experiment 4 was the test run conducted during the highest average wind speeds, as shown in Appendix A. Convection and conduction heat losses are directly related to wind speed and direction, and as a result, an increase in wind speed will drastically increase heat losses from the receiver. The effect thereof is shown in Fig. 20 and is illustrated by the irregular temperatures (uneven slope) during heat-up (in both the experimental and predicted temperatures), as well as a longer heat-up when compared to Experiment 3 even though a similar average DNI was recorded. This negatively affected the heat-up time, and less molten material was drained from the receiver during this experiment. The analytical model results shown in Fig. 20 again illustrate that the experiment was stopped prematurely and that more heating was required to melt the entire zinc batch. Erratic temperature measurements around the two-and-a-quarter hour mark resulted in temperatures above 720 K and as per the experimental procedure, served as an indication to drain the zinc cavity. These temperature spikes are likely due to localized heating, either caused by insufficient mixing by the rotational movement of the receiver or by the inconsistent temperature profiles in the cavity receiver due to the higher wind speeds, at which forced convection becomes the driving heat loss mechanism [27]. In order to match the predictive model to the experimental zinc temperatures, a heat transfer efficiency constant of $c = 0.8$ was required. At higher-than-average wind speeds, it was still possible to match the predictive zinc temperature to that of the experimental results, which again speaks to the accuracy of the analytical model. The reason for the required heat transfer efficiency constant is that a significant volume of zinc was drained during Experiment 3, which was then replaced with new zinc feedstock. The internal walls of the receiver were still coated with a layer of solid zinc from the previous experiment and this layer of process material aided in the heat transfer between the receiver cavity wall and the zinc feedstock. A heat transfer efficiency constant of $c = 0.8$ will, therefore, likely be the best approximation when evaluating the day-to-day operation of this technology.

4.2.5. Comparison with Experiment 5

Experiment 5, shown in Fig. 21, was executed using a new receiver vessel, a new set of thermocouples, and a fresh batch of zinc feedstock. Significant temperature variations were noticed in the difference between the receiver and zinc temperatures and between the receiver temperatures themselves. The variation between the receiver temperatures is possibly due to localized heating in the zinc particles, resulting in better contact with the receiver wall in some places than others. This theory is confirmed by the fact that the temperatures converge as soon as the melting temperature of zinc is reached, which indicates that the zinc is softening and is now making good contact with the side wall of the receiver. Also, as opposed to the previous experiment, the wall of the zinc cavity was not lined with a layer of solidified process material from a previous experiment. This omission negatively affected the heat transfer between the receiver cavity wall and the zinc. During Experiment 5, the lowest wind speed out of all the experiments was recorded, and at these wind speeds, natural convection is the driving force for convection heat losses. A heat transfer efficiency constant of $c = 0.6$ was required to match the predictive model to the experimental results. This heat transfer efficiency constant will typically be representative of the first batch of zinc processed in a new receiver when evaluating the technology as an industrial application. After the first batch, the heat transfer efficiency constant can be adjusted to $c = 0.8$, as was determined by Experiment 3.

4.3. Discussion

The results have shown that it is not only possible to melt zinc using CSP only, but a predictive analytical model can, within a few minutes of accuracy, predict when a batch of zinc inventory will be completely molten. The comparative results shown in Figs. 17–21 speak to the accuracy of the analytical model and that it can be used to investigate this technology application further.

When the analytical model is broken down into the individual heat loss components, more detail can be provided into which heat loss mechanism has the most significant influence on the system's efficiency. The heat balance of Experiment 3, shown in Fig. 22, indicates that the conduction and radiation heat losses stay relatively constant throughout the experiment, but the convection heat loss is very erratic. The erratic behaviour of the convection heat loss mechanism is related to the variability in the wind speed and direction, and depending on the wind speed, this heat loss mechanism is either driven by natural convection, forced convection, or a combination of both. The variability in the heat losses also resulted in the system's efficiency following the same trend. The average overall efficiency obtained for Experiment 3 was 42.14 % (see Fig. 22), but the efficiency varied from 82 % to as low as −56 %. Negative efficiencies point to a situation where the heat loss exceeds the heat input, and the system is losing energy, instead of gaining energy required to melt the zinc inventory (typically during a wind gust). The

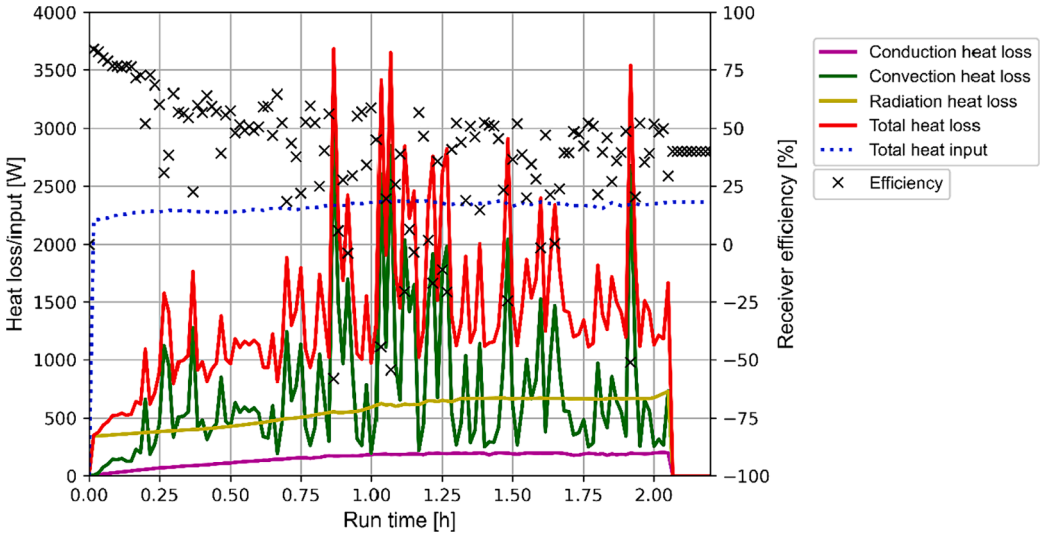

Fig. 22. Experiment 3 heat input and heat loss mechanisms are shown together with the instantaneous efficiency of the system.

achieved efficiency compares well, but exceeds, the melting efficiency of between 22 % and 36 % obtained by Demirtaş and Özcan [19] in a similar solar melting study. The results obtained by investigating the individual heat loss mechanisms show that the convection heat loss is the most unpredictable and has one of the largest influences on the system's efficiency. This statement, in turn, demonstrates the significant effect environmental conditions, such as wind speed and direction, have on the overall efficiency and stability of this technology application. This significant influence is why not only solar input and ambient conditions need to be considered when evaluating CSP technologies for melting applications but also factors such as wind speed and direction.

When the heat losses for Experiment 5 are observed, as shown in Fig. 23, much more stability is noticed. This is attributed to much lower wind speeds and resulted in natural convection being the driving mechanism for convection heat loss. Natural convection results in smaller heat losses for the convection heat loss mechanism, and as a result, much lower total heat losses were recorded. Even though much more stable heat losses were recorded, resulting in more stable efficiencies, the average efficiency for Experiment 5 was only 26.26 %. The likely reason for this is the weak internal heat transfer between the receiver cavity wall and the zinc feedstock, which resulted in a lower heat transfer efficiency constant of $c = 0.6$ to be considered. Operational issues during this test and the loss of collector surface during the test caused the variability in the total heat input to the system. Fig. 23 again demonstrates the large influence that the wind speed and direction have on the system's overall stability.

5. Case study

This study aimed to demonstrate that it is possible to melt zinc metal using only a CSP input and to develop an analytical model that can be used as a tool to develop this technology application further. The remelting of zinc cathodes, produced during the hydro-metallurgical production of zinc, has been identified as a suitable application to apply CSP to a high-temperature industrial application. This melting process forms part of the last step in the Roast-Leach-Electrowin (RLE) process. This step is conventionally done by melting the zinc cathodes in induction furnaces. At the time of writing, South Africa had no active zinc producing plants, making this application more favourable in the South African context by allowing this metal to be beneficiated locally using the country's excellent solar resource.

The analytical model uses historical weather conditions as an input to predict the number of zinc batches that can be processed in a day. Between 07:00 and 17:00, a full-day run on the 16th of August 2022 at Pretoria (South Africa) could produce two molten batches of zinc, as shown in Fig. 24. With 17 kg of zinc processed during each batch, and

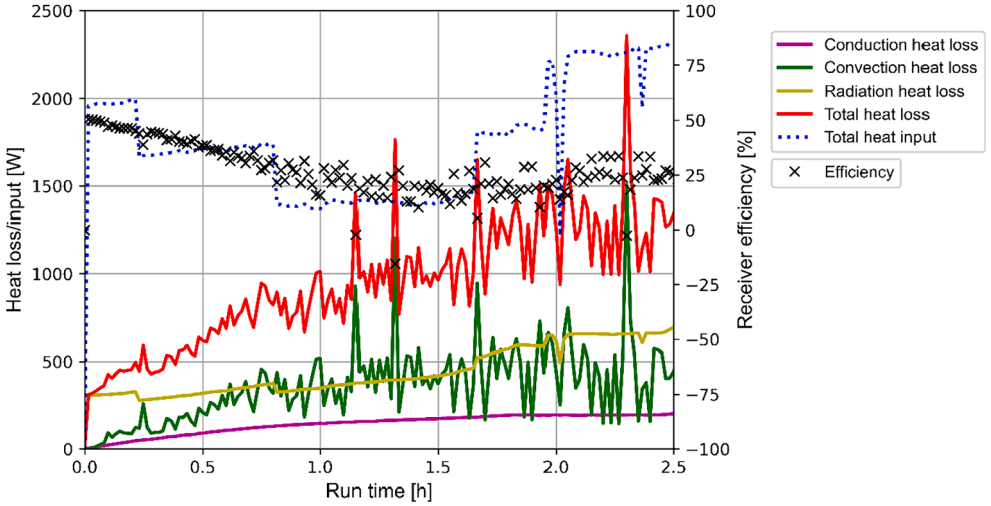

Fig. 23. Experiment 5 heat input and heat loss mechanisms are shown together with the instantaneous efficiency of the system.

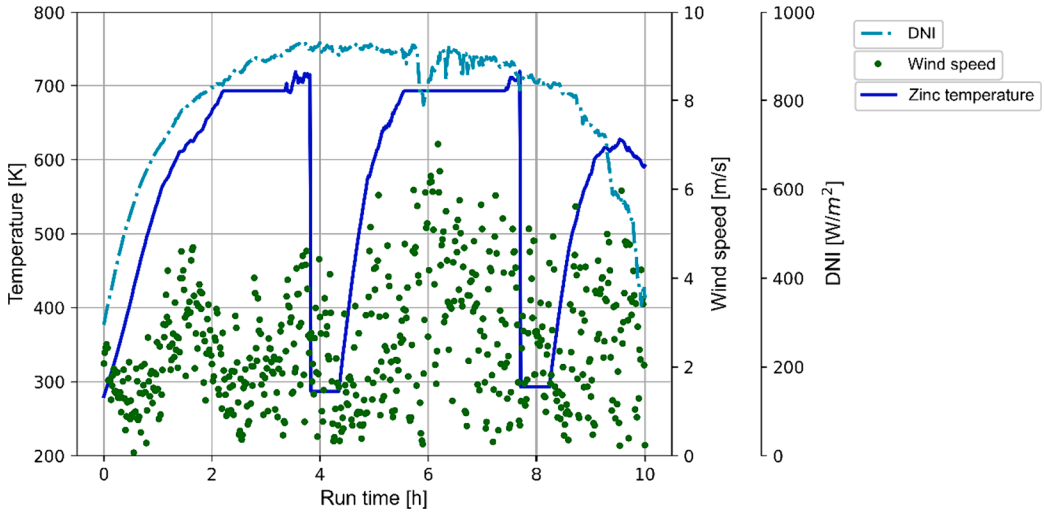

Fig. 24. Batch throughput results with DNI and wind speed [49] for the 16th of August 2022 at Pretoria, South Africa.

with 80 % being tapped, just over 27 kg of molten zinc could be produced during this day, using the tested receiver design. The batch throughput is not only dependent on the solar quality but also on the wind and ambient temperature conditions, as was discussed in the analytical model section.

The environmental influence is evident when Fig. 25 is observed, during which the analytical model was re-executed with the weather conditions of the 5th of September 2022 at the same location as for Fig. 24. The same analytical model was used, assuming the same heat transfer efficiency constant of $c = 0.8$, as determined for day-to-day operations, with the only difference being the weather conditions. On the 5th of September 2022, three complete batches could be processed, resulting in approximately 41 kg of tapped zinc, even though a slightly weaker solar irradiance was recorded on this day. These results again point to the significant influence the wind conditions have on the efficiency of the melting process and as a result, the throughput of this technology application. In average wind speeds of below 2 m/s, the experimental setup in Pretoria therefore has the potential to process 14.4 kg zinc per day per m^2 of solar collector surface during the spring season, providing an indication of the expected average daily performance over a typical year.

To further demonstrate the benefit of using CSP for small-scale to medium-scale batch processing of zinc, these results can be compared with more conventional heat sources. Induction furnaces as well as gas burners can be used for the melting of zinc metal [11], to produce molten zinc for downstream processes such as casting, as mentioned for the RLE process, or recycling applications. Firstly, considering a small-scale induction furnace with a capacity of housing 15 kg of material, around 600 kWh per ton of electrical power would be required, taking into account an energy efficiency of 70 % [57]. This would result in an energy requirement of 0.6 kWh/kg of processed zinc, or 24.6 kWh/day to process the same mass of 41 kg as mentioned in the example above. Furthermore, considering that power in South Africa is mostly generated by coal-fired power stations, and assuming a CO_2 emission rate of 0.87 kg CO_2/kWh [58], 0.52 kg CO_2 is emitted for every kilogram of zinc that is processed. This results in 21.3 kg of CO_2 emissions being generated, per day, to produce the same volume of molten zinc as with the solar receiver discussed in this study.

In terms of equipment costs, the solar receiver prototype design used for this study had a total fabrication cost of approximately 515 USD. This cost included the steelwork, insulation material, drive system, as well as the instrumentation required. To put this into perspective, a small-scale induction furnace with a 15 kg capacity costs upwards of 5000 USD [59]. The CSP system can therefore be a cost-effective and feasible alternative as long as the solar dish setup and receiver combination costs less than 5000 USD.

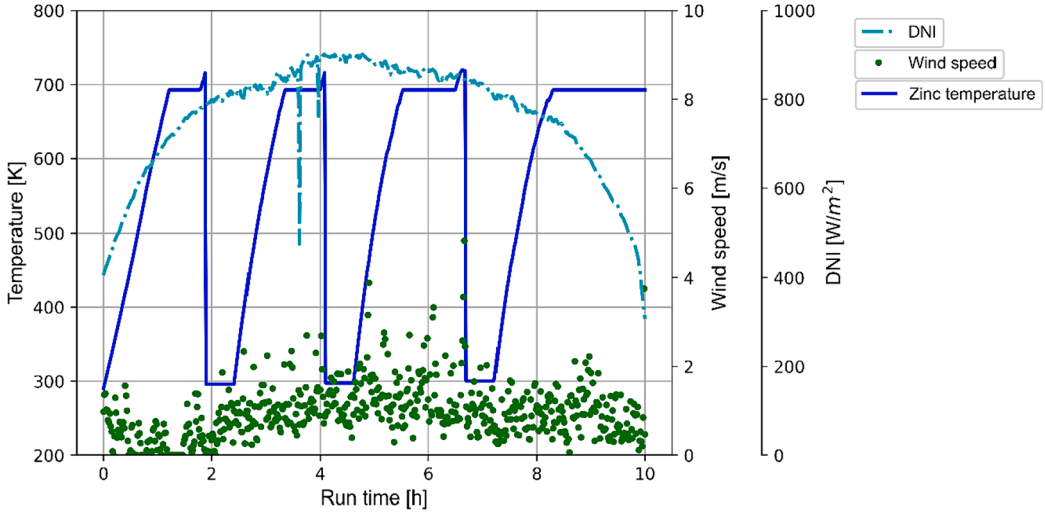

Fig. 25. Batch throughput results with DNI and wind speed [49] for the 5th of September 2022 at Pretoria, South Africa.

The case study highlights the benefit of making use of CSP as the heat source to melt zinc, not only from an environmental perspective but also from a financial point of view. These results motivate further development of this technology application. The analytical model as well as the high-level cost-saving analysis can be used to evaluate the potential for making use of CSP in industrial applications such as the beneficiation of local zinc resources. The concept of remelting zinc metal has been demonstrated, however, a more detailed financial evaluation is required in future work to determine the feasibility of applying this technology to the conventional zinc metal flowsheet.

6. Conclusion

For the melting of zinc metal, gas-fired, coal-fired and electric furnaces can result in significant energy costs. This research study presented an experimental investigation into the use of concentrated solar power as an alternative heat source for melting zinc metal. A cylindrical cavity receiver and a multi-faceted parabolic dish setup was considered and experimentally demonstrated. To successfully prove the technology application, and to provide insight into its operational requirements and feasibility, five experimental runs were executed. Four of these experiments produced molten zinc and demonstrated that it is possible to melt zinc using only concentrated solar power. The thermal efficiency of the receiver was calculated to be in the range of 42 %, which compares well with the literature [19]. To facilitate the development of this technology for industrial heat applications, a predictive analytical model was developed and validated. Each experimental test provided valuable data against which the predictive analytical model could be validated. The analytical model developed as part of this study uses historical solar and weather data as input and can be used to further refine the design employed and as a tool to investigate the feasibility of this technology application for various locations. The analytical model, in combination with the experimental results, has shown that 14.4 kg of zinc can be processed in a typical day for each m^2 of parabolic dish reflector area.

A high-level case study demonstrated the value of this technology application in the hydro-metallurgical production of zinc (remelting of zinc cathodes as part of the Roast-Leach-Electrowin process). Not only can up to 0.52 kg of CO_2 emissions be avoided for every kilogram of zinc being processed, but this technology application also unlocks significant energy cost savings. 0.6 kWh/kg processed zinc is saved when compared to conventional induction furnace technology. The low cost and modularity associated with the design of this CSP system can also make this technology application an attractive alternative for low-income or rural users without access to cost-effective power. It can allow entrepreneurs access to small/medium-scale recycling, galvanisation, metal die-casting and melting applications, which otherwise might not have been feasible.

6.1. Recommendations for future work

- Additional research into the influence of wind speed and direction, relative to the receiver aperture, is required to further refine the forced convection heat loss estimation. The model employed for this study served as a sound basis and considered both wind speed and the wind direction. However, this work still has limited validation, and the model employed was developed for a different receiver and solar collector design. A better understanding of the mechanisms at play during the transition from natural to forced convection, or the combination thereof, is still required.
- The heat transfer mechanisms in the zinc feedstock and their influence on the greater heat balance should be investigated in greater detail. The effect of heat transfer within the zinc feedstock was not modelled but was determined through experimental work. It was found that the heat transfer efficiency constant (c) for a new batch and a new receiver vessel is in the range of 0.6. Once a molten batch has been achieved with the receiver, which will be the case for the day-to-day operation of this technology application, a heat transfer efficiency constant of $c \approx 0.8$ was determined. This heat transfer efficiency constant considers that a coating of process material remained in the receiver after the previous batch of zinc was drained, on top of which a new batch is added. The new batch will result in several voids in the inventory, but the surface coating will aid in the initial heat transfer. A heat transfer efficiency constant of $c = 1$ can only be assumed when a solid zinc inventory is used. Therefore, the heat transfer efficiency constant (c) also correlates with the mass of zinc in the receiver during the experimental run. Considering that the mass of the receiver vessel is also included during the sensible heating phase, the ratio of steel to zinc changes as less or more zinc is charged to the zinc container. The use of the zinc mass as an indication of the heat transfer efficiency constant (c), based on a zinc-to-steel ratio or the air void volume due to the mass of zinc charged, can also be considered in a future study.
- The knowledge generated by demonstrating the melting of zinc metal using CSP can serve as the basis for various other zinc metal-related research including, but not limited to, metal phase-change studies, solar galvanisation, and thermal storage. This research can also be applied to other low-melting-point metal processing applications, including casting and recycling.

Declaration of competing interest

The authors declare that they have no known competing financial interests or personal relationships that could have appeared to influence the work reported in this paper.

Data availability

Data will be made available on request.

Acknowledgements

This paper is published with the permission of Mintek and Tenova Pyromet. The authors would like to acknowledge the support of SAURAN, allowing for the continuous development of solar thermal technology in Southern Africa by providing accurate weather data. The authors would also like to acknowledge the work done by previous postgraduate students at the University of Pretoria that aided in the development of the multi-facet parabolic dish design, which ultimately resulted in the versatile facility used for executing this study. The authors express their gratitude to the Renewable Energy Hub and Spokes Programme of the Department of Science and Innovation (DSI), South Africa, for financial support through the UP Solar Thermal Spoke. Lastly, the authors acknowledge R. Fondse, M.G. Kotze, and W.G. le Roux for sponsoring the solar tracking system.

Appendix A

Table A1
Comparison between the different experimental test runs (with minimum and maximum recorded values). Wind speeds of up to 8.39 m/s have been demonstrated for this receiver design. The analytical model will become unstable when the Rayleigh number exceeds 1012 (the convection model becomes invalid) which is dependent on both the receiver design and environmental conditions. No limitations on DNI inputs have been found and ambient temperatures below freezing point will require additional validation. Zinc mass and the heat transfer in between particles require further investigation, as the model considers perfect contact between the zinc inventory and receiver sidewall. A heat transfer efficiency constant has been proposed to account for voids but has only been done for as low as 50 % volume fill.

		Parameter												
		Zinc mass (m)	Volume fill	Average DNI (I)	Average Temp. (T_∞)	Average wind speed (V_{wind})	Average receiver tilt angle (θ)	Average wind direction relative to the receive aperture (φ)	Heat transfer efficiency constant (c)	Average wind direction classification	Faceplate insulation	Feedstock shape inside cavity	Date	Time of day	Duration
		kg	%	W/m^2	°C	m/s	deg	deg		(−30° < head on < 30°) [27]	YES/NO	Based on the previous experiment			Minutes
Experiment no.	*1*	10	47.62	688.57	18.55	2.01	56.28	50.81	0.5	Side-on-wind	NO	New charge with no previous melt	26/07/2022	13:37–15:25	109
	2	10	47.62	792.61	16.78	2.68	45.41	50.23	0.4	Side-on-wind	NO	Charge from Exp 1.	04/08/2022	10:12–13:00	169
	3	16.96	80.76	909.98	14.2	2.14	44.75	11.51	1	Head-on-wind	YES	Good contact with sidewall due to molten material from Exp 2.	16/08/2022	09:32–12:25	174
	4	14.53	69.19	908.39	12.03	5.26	45.91	61.83	0.8	Side-on-wind	YES	Most of the zinc was drained during Exp 3, so new charge material was added. Some molten material left over from Exp 3 results in better contact between Zn and thermocouples.	21/08/2022	09:11–11:53	163
	5	10	47.62	835.67	23.65	0.95	45.23	−38.68	0.6	Side-on-wind	YES	New receiver and charge with no previous melt.	05/09/2022	08:36–11:30	175
Min		10	47.62	475	9.02	0.001	32.09	−89.63	0.4	–	–	–	–	–	109
Max		16.96	80.76	936	28.34	8.36	60.61	81.54	1	–	–	–	–	–	175

References

[1] C. Philibert, Renewable Energy for Industry, IEA, Paris, 2017 [Online], Available: https://www.iea.org/reports/renewable-energy-for-industry.
[2] M. Azadi, S.A. Northey, S.H. Ali, M. Edraki, Transparency on greenhouse gas emissions from mining to enable climate change mitigation, Nat. Geosci. 13 (2) (2020) 100–104, https://doi.org/10.1038/s41561-020-0531-3.
[3] S.A. Kalogirou, Solar thermal collectors and applications, Prog. Energy Combust. Sci. 30 (3) (2004) 231–295, https://doi.org/10.1016/j.pecs.2004.02.001.
[4] L. Kumar, M. Hasanuzzaman, N.A. Rahim, Global advancement of solar thermal energy technologies for industrial process heat and its future prospects: a review, Energy Convers. Manag. 195 (2019) 885–908, https://doi.org/10.1016/j.enconman.2019.05.081.
[5] L.G. Rosa, Solar heat for materials processing: a review on recent achievements and a prospect on future trends, ChemEngineering 3 (4) (2019) 83, https://doi.org/10.3390/chemengineering3040083.
[6] Zinc Statistics and Information, Accessed: Feb. 16, 2021 [Online], Available: https://www.usgs.gov/centers/nmic/zinc-statistics-and-information.
[7] S. Mohale et al., South African mineral industry 2013–2014, Department of Mineral Resources - Republic of South Africa, Pretoria, 2015, ISBN: 978-0-621-43629-7.
[8] Kirk and Othmer, Encyclopedia of Chemical Technology, John Wiley & Sons, Inc., 2000.
[9] World Bank Group, Solar resource maps of South Africa, SOLARGIS. Accessed: Feb. 15, 2021 [Online], Available: https://solargis.com/maps-and-gis-data/download/south-africa.
[10] K.K. Sahu, A. Agrawal, Lead zinc extraction processes, in: Proceedings on Extraction of Nonferrous Metals and their Recycling, Jamshedpur, 2008, pp. 57–70.
[11] J.P. van Dyk, An Overview of the Zincor Process, South African Institute of Mining and Metallurgy, Johannesburg, South Africa, Mar. 2006.
[12] N.A. Sithole, L. Hockaday, P.J.A. Bezuidenhout, Solar energy for greener zinc processing in South Africa, in: IMPC 2020 Congress Proceedings, The Southern African Institute of Mining and Metallurgy, Cape Town, South Africa, Oct. 2020, pp. 3779–3791.
[13] T. Bergman, A. Lavine, F. Incropera, D. Dewitt, Fundamentals of Heat and Mass Transfer, 7th ed., Hohn Wiley & Sons, USA, 2011.
[14] J. Coventry, C. Andraka, Dish systems for CSP, Sol. Energy 152 (2017) 140–170, https://doi.org/10.1016/j.solener.2017.02.056.
[15] Z. Chongzhe, et al., Design and optimization of a high-temperature cavity receiver for a solar energy cascade utilization system, Renew. Energy 102 (2016), https://doi.org/10.1016/j.renene.2016.11.044.
[16] A. Singh, S.K. Natarajan, Comparative study of modified conical cavity receiver with other receivers for solar parabolic dish collector system, Res. Sq. (2021), https://doi.org/10.21203/rs.3.rs-237950/v1.
[17] A. Kasaeian, A. Kouravand, M.A. Vaziri Rad, S. Maniee, F. Pourfayaz, Cavity receivers in solar dish collectors: a geometric overview, Renew. Energy 169 (2021) 53–79, https://doi.org/10.1016/j.renene.2020.12.106.
[18] E. Bellos, E. Bousi, C. Tzivanidis, S. Pavlovic, Optical and thermal analysis of different cavity receiver designs for solar dish concentrators, Energy Convers. Manag. X 2 (2019) 100013, https://doi.org/10.1016/j.ecmx.2019.100013.
[19] C. Demirtas, A.K. Ozcan, The experimental thermal analysis of aluminum metal melting with concentrated solar energy, Sol. Energy Mater. Sol. Cells 222 (2021) 1–13, https://doi.org/10.1016/j.solmat.2020.110940.
[20] A. Ahmadi Balootaki, A. Karimipour, D. Toghraie, Nano scale lattice Boltzmann method to simulate the mixed convection heat transfer of air in a lid-driven cavity with an endothermic obstacle inside, Phys. Stat. Mech. Appl. 508 (2018) 681–701, https://doi.org/10.1016/j.physa.2018.05.141.
[21] S. Dabiri, E. Khodabandeh, A.K. Poorfar, R. Mashayekhi, D. Toghraie, S.A. Abadian Zade, Parametric investigation of thermal characteristic in trapezoidal cavity receiver for a linear Fresnel solar collector concentrator, Energy 153 (2018) 17–26, https://doi.org/10.1016/j.energy.2018.04.025.
[22] R.Y. Ma, Wind Effects on Convective Heat Loss from a Cavity Receiver for a Parabolic Concentrating Solar Collector, Sandia Laboratory, California State Polytechnic University, California, SAND92-7293, 1993.
[23] T. Taumoefolau, S. Paitoonsurikarn, G. Hughes, K. Lovegrove, Experimental investigation of natural convection heat loss from a model solar concentrator

cavity receiver, J. Sol. Energy Eng. 126 (2) (2004) 801–807, https://doi.org/10.1115/1.1687403.
[24] T. Yazdanipour, F. Shahraki, D.M. Kalhori, Experimental analysis of free convection heat loss in a bicylindrical cavity receiver, Therm. Sci. Eng. Prog. 20 (2020) 100663, https://doi.org/10.1016/j.tsep.2020.100663.
[25] E. Abbasi-Shavazi, J.F. Torres, G. Hughes, J. Pye, Experimental correlation of natural convection losses from a scale-model solar cavity receiver with non-isothermal surface temperature distribution, Sol. Energy 198 (2020) 355–375, https://doi.org/10.1016/j.solener.2020.01.023.
[26] M. Uzair, T.N. Anderson, R.J. Nates, Modeling of convective heat loss from a cavity receiver coupled to a dish concentrator, Sol. Energy 176 (2018) 496–505, https://doi.org/10.1016/j.solener.2018.10.060.
[27] K.S. Reddy, G. Veershetty, T. Srihari Vikram, Effect of wind speed and direction on convective heat losses from solar parabolic dish modified cavity receiver, Sol. Energy 131 (2016) 183–198, https://doi.org/10.1016/j.solener.2016.02.039.
[28] M. Prakash, S.B. Kedare, J.K. Nayak, Investigations on heat losses from a solar cavity receiver, Sol. Energy 83 (2) (2009) 157–170, https://doi.org/10.1016/j.solener.2008.07.011.
[29] R.D. Jilte, S.B. Kedare, J.K. Nayak, Investigation on convective heat losses from solar cavities under wind conditions, Energy Proc. 57 (2014) 437–446, https://doi.org/10.1016/j.egypro.2014.10.197.
[30] K.L. Lee, A. Chinnici, M. Jafarian, M. Arjomandi, B. Dally, G. Nathan, Experimental investigation of the effects of wind speed and yaw angle on heat losses from a heated cavity, Sol. Energy 165 (2018) 178–188, https://doi.org/10.1016/j.solener.2018.03.023.
[31] S.-Y. Wu, F.-H. Guo, L. Xiao, Numerical investigation on combined natural convection and radiation heat losses in one side open cylindrical cavity with constant heat flux, Int. J. Heat Mass Transf. 71 (2014) 573–584, https://doi.org/10.1016/j.ijheatmasstransfer.2013.12.064.
[32] S.-Y. Wu, L. Xiao, Y. Cao, Y.-R. Li, Convection heat loss from cavity receiver in parabolic dish solar thermal power system: a review, Sol. Energy 84 (8) (2010) 1342–1355, https://doi.org/10.1016/j.solener.2010.04.008.
[33] T. Hahm, H. Schmidt, B. Lebmann, A cone concentrator for high-temperature solar cavity receivers, Sol. Energy 65 (1) (1999) 33–41, https://doi.org/10.1016/S0038-092X(98)00119-4.
[34] L.C. Ngo, T. Bello-Ochende, J.P. Meyer, Three-dimensional analysis and numerical optimization of combined natural convection and radiation heat loss in solar cavity receiver with plate fins insert, Energy Convers. Manag. 101 (2015) 757–766, https://doi.org/10.1016/j.enconman.2015.05.061.
[35] K.B. Watson, B.G. Cannon, M. Bosman, H. Li, Welding consumables for galvanising kettles, Australian Welding Journal 46 (Fourth Quarter) (2001) 33–38.
[36] S.G. Blakey, S.B.M. Beck, The effect of combined radiation and convection on hot dip galvanizing kettle wear, Appl. Therm. Eng. 24 (8–9) (2004) 1301–1319, https://doi.org/10.1016/j.applthermaleng.2003.11.025.
[37] G. Vourlias, N. Pistofidis, D. Chaliampalias, E. Pavlidou, G. Stergioudis, On the corrosion mechanism of zinc pack coatings deposited on low carbon steel: results of laboratory tests, Corros. Eng. Sci. Technol. 42 (2) (2007) 152–160, https://doi.org/10.1179/174327807X159899.
[38] D. Apelian, M. Paliwal, D.C. Herrschaft, Casting with zinc alloys, JOM 33 (11) (1981) 12–20, https://doi.org/10.1007/BF03339527.
[39] G. Kong, R. White, Toward cleaner production of hot dip galvanizing industry in China, J. Clean. Prod. 18 (2010) 1092–1099, https://doi.org/10.1016/j.jclepro.2010.03.006.
[40] P.J.A. Bezuidenhout, W.G. Le Roux, J.D. Steenkamp, Experimental analysis of zinc melting using CSP, in: Advances in Pyrometallurgy, in the Minerals Metals & Materials Series, Springer Nature Switzerland, Cham, 2023, pp. 225–235, https://doi.org/10.1007/978-3-031-22634-2_21.
[41] Sundog, EverBright | SundogSolarTech | Arvada, SundogSolarTech. Accessed: Oct. 16, 2022 [Online], Available: https://www.sundogsolartech.com.
[42] C. Roosendaal, J.K. Swanepoel, W.G. Le Roux, Performance analysis of a novel solar concentrator using lunar flux mapping techniques, Sol. Energy 206 (2020) 200–215, https://doi.org/10.1016/j.solener.2020.05.050.
[43] J.K. Swanepoel, W.G. le Roux, A.S. Lexmond, J.P. Meyer, Helically coiled solar cavity receiver for micro-scale direct steam generation, Appl. Therm. Eng. 185 (2021) 116427, https://doi.org/10.1016/j.applthermaleng.2020.116427.
[44] J.K. Swanepoel, C. Roosendaal, W.G. le Roux, Photogrammetry analysis of a vacuum-membrane solar dish using elliptical television antennas, in: presented at the SOLARPACES 2020: 26th International Conference on Concentrating Solar Power and Chemical Energy Systems, Freiburg, Germany, 2022, p. 120021, doi: 10.1063/5.0087025.
[45] G. Zanganeh, A. Pedretti, S. Zavattoni, M. Barbato, A. Steinfeld, Packed-bed thermal storage for concentrated solar power – pilot-scale demonstration and industrial-scale design, Sol. Energy 86 (10) (2012) 3084–3098, https://doi.org/10.1016/j.solener.2012.07.019.
[46] R.C. Gee, Development of an Abrasion-Resistant Antisoiling Coating for Front-Surface Reflectors - Sundog Solar Technologies, SunShot Incubator Program, Arvada, DE-EE0006696, 2017 [Online], Available: https://www.osti.gov/servlets/purl/1371550.
[47] Raspberry Pi Ltd, Raspberry Pi, Raspberry Pi [Online], Available: https://www.raspberrypi.com/.
[48] Measurement Computing Corporation, Thermocouple Measurement HAT for Raspberry Pi® from Measurement Computing, MC Measurement Computing - MCC 134 [Online], Available: https://www.mccdaq.com/DAQ-HAT/MCC-134.aspx.
[49] M. J. Brooks et al., SAURAN: a new resource for solar radiometric data in Southern Africa, J. Energy South. Afr. 26(1) (2015), doi: 10.17159/2413-3051/2015/v26i1a2208.
[50] Welcome to Python.org, Python.org, Accessed: Oct. 09, 2022 [Online], Available: https://www.python.org/.
[51] L.S.M. Castellanos, G.E.C. Caballero, V.R.M. Cobas, E.E.S. Lora, A.M.M. Reyes, Mathematical modeling of the geometrical sizing and thermal performance of a Dish/Stirling system for power generation, Renew. Energy 107 (2017) 23–35, https://doi.org/10.1016/j.renene.2017.01.020.
[52] R.E. Hogan, AEETES - a solar reflux receiver thermal performance numerical model, Sol. Energy 52 (2) (1994) 167–178, https://doi.org/10.1016/0038-092x(94)90066-3.
[53] Anvils South Africa, Technical Data Sheet - Ceramic Fibre Blanket, Anvils South Africa, 2022 [Online], Available: https://www.anvils.co.za/product/ceramic-fibre-blanket-insulation/.
[54] J.A. Harris, T.G. Lenz, Thermal performance of solar concentrator-cavity receiver systems, Sol. Energy 34 (2) (1985) 135–142, https://doi.org/10.1016/0038-092x(85)90170-7.
[55] H. Sadiq, M.B. Wong, J. Tashan, R. Al-Mahaidi, X.-L. Zhao, Determination of steel emissivity for the temperature prediction of structural steel members in fire, J. Mater. Civ. Eng. 25 (2) (2013) 167–173, https://doi.org/10.1061/(ASCE)MT.1943-5533.0000607.
[56] S. Sarkar, M. Gopinath, S.S. Chakraborty, B. Syed, A.K. Nath, Analysis of temperature and surface hardening of low carbon thin steel sheets using Yb-fiber laser, Surf. Coat. Technol. 302 (2016) 344–358, https://doi.org/10.1016/j.surfcoat.2016.06.045.
[57] J. Schifo, J. Radia, Theoretical/best practice energy use in metalcasting operations, Advanced Technology Institute North Charleston, Washington, 2004. doi: 10.2172/1216246.
[58] Climate Transparency Report 2022 - South Africa, Climate Transparency.org, Oct. 2022 [Online], Available: https://www.climate-transparency.org/wp-content/uploads/2022/10/CT2022-South-Africa-Web.pdf.
[59] Mini-Melt® Furnaces | Small Capacity Induction Furnace, Inductotherm Corp [Online], Available: https://www.inductotherm.com/products/mini-melt-furnaces/.